Review

Development and Applications of Thermoelectric Oxide Ceramics and Devices

Ping Zhang [1] , **Zhihao Lou** [1], **Lingyun Gong** [1], **Zhuozhao Wu** [2], **Xuanjie Chen** [2], **Weihang Xu** [2], **Yiqi Wang** [2],
Jie Xu [1,*] , **Zinovi Dashevsky** [3] **and Feng Gao** [1,*]

[1] State Key Laboratory of Solidification Processing, MIIT Key Laboratory of Radiation Detection Materials and Devices, NPU-QMUL Joint Research Institute of Advanced Materials and Structure, USI Institute of Intelligence Materials and Structure, School of Materials Science and Engineering, Northwestern Polytechnical University, Xi'an 710072, China; amyzp9305@mail.nwpu.edu.cn (P.Z.)

[2] Queen Mary University of London Engineering School, Northwestern Polytechnical University, Xi'an 710072, China

[3] Department of Materials Engineering, Ben-Gurion University of the Negev, Beer-Sheva 84105, Israel

* Correspondence: xujie@nwpu.edu.cn (J.X.); gaofeng@nwpu.edu.cn (F.G.)

Abstract: Thermoelectric materials have gained wide attention to realize multilevel efficient energy management to alleviate the increasingly severe energy crisis. Oxide ceramics were well-explored as potential thermoelectric candidates because of their outstanding merits, including abundance, eco-friendliness, high-temperature stability, and chemical stability. In this work, we aim to provide a comprehensive summary of the diversified state-of-the-art oxide ceramics and establish the links between composition designing, preparation process, structural characteristics, and properties to summarize the underlying chemistry and physics mechanism of band engineering, doping, composited with the second phase, defects engineering, and entropy engineering. Furthermore, advanced device design and applications such as thermoelectric modules, miniature generators, sensors, and coolers were reviewed. Ultimately, the challenges and future perspective of oxides ceramics for the device design and thermoelectric applications in the development of energy harvesting technology have been prospected.

Keywords: thermoelectrics; oxides ceramics; ZT; electrical conductivity; phonon scattering

1. Introduction

The escalating energy demand and the decreasing fossil energy make countries all over the world devoted to exploring new types of energy. At the same time, researchers are working on ways to maximize the utilization efficiency of traditional non-renewable energy. Thermoelectric materials (TEs) have been used as a potential energy harvesting technology because they can convert heat into electricity and have no requirements for waste heat temperature [1–3]. Thermoelectric devices generally consist of *n*-type and *p*-type TEs wired electrically in series (or partly parallel) and thermally in parallel. Furthermore, there are also thermoelectric devices with single n-type and p-type TEs. They have the advantages of no moving parts, no noise, small size, etc., and have significant application merits in the military, aerospace, and high-tech energy fields [4,5].

It has been more than 200 years since the thermoelectric effect was discovered, and people have been constantly exploring and developing its industrial applications. In the early 1920s, Altenkirch, a German physicist, developed the fundamentals of thermoelectric power generation and refrigeration and summarized the performance evaluation parameters of TEs [6]: electrical conductivity (σ), Seebeck coefficient (S), and thermal conductivity (κ). Dimensionless thermoelectric merit ($ZT = S^2\sigma T/\kappa$, S is Seebeck coefficient, σ is electrical conductivity, T is absolute temperature, κ is thermal conductivity) is usually used as an indicator to measure the thermoelectric performance [7]. TEs with large ZT values must meet the requirements of a high Seebeck coefficient to ensure the generation

of the obvious thermoelectric effect—high electrical conductivity leading to small Joule heat, large output power, as well as low thermal conductivity, are required to generate a substantial temperature difference. The above three thermoelectric parameters have a strong coupled relationship because they are dependent on the carrier concentration in a conflicting manner that restricts and influences each other, making how to optimize thermoelectric performance a huge challenge. Therefore, the coordinated regulation of *S*, *σ*, and *κ* to improve *ZT* has become the key point to realize the industrial application of thermoelectric materials.

At present, research on Bi_2Te_3, PbTe, and Si-Ge alloy semiconductor TEs is relatively extensive, and the manufactured thermoelectric devices by the theses Bi_2Te_3 or PbTe TEs exhibit high conversion efficiency. Oxide TEs have attracted increasing attention for their merits of stable crystal structure, good oxidation resistance, chemical stability, and being environmentally friendly [8,9]. They can effectively use high-temperature exhaust heat to generate electricity to improve the comprehensive efficiency of energy utilization and are, therefore, considered to be a class of functional materials with great application prospects. Due to the small carrier concentration in oxide TEs, their *ZT* values are lower than those of metal or alloy TEs, which has attracted much interest from researchers to regulate and improve the thermoelectric performance of oxide materials through various strategies.

Environmentally friendly oxides TEs that can be used in high temperatures have emerged as the times require. The *p*-type TEs include $Ca_3Co_4O_9$ [10–15], Na_xCoO_2 [16–19], and BiCuSeO [20–22]. The *n*-type TEs contain $SrTiO_3$ [23–27], $CaMnO_3$ [28,29], $CaTiO_3$ [30,31], In_2O_3 [32,33], and ZnO [34,35], etc. As presented in Figure 1, most *ZT* values of the oxide TEs are smaller than 1.0 and have an urgent demand for optimizing their performance to meet the broad and efficient recycling of energy.
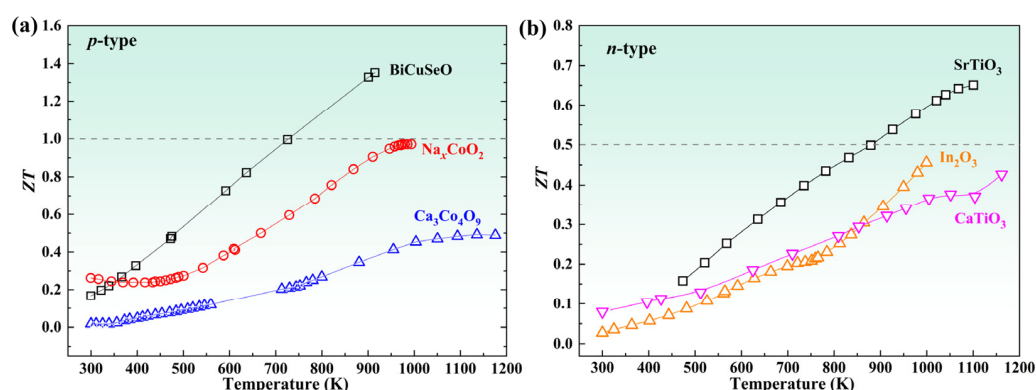

Figure 1. The figure of merit *ZT* for state-of-the-art *p*-type [12,18,20] (**a**) and *n*-type [30,33,36] (**b**) oxide materials used in high-temperature.

2. Thermoelectric Fundamentals and Thermoelectric Parameters

Thermoelectric materials utilize the thermoelectric effect to achieve direct heat-to-electricity conversion. As shown in the schematic diagrams in Figure 2, the thermoelectric effect includes three effects: (i) the Seebeck effect, which transforms heat into electricity; (ii) the Peltier effect, absorption or release of heat at a junction in which there is an electric current; and (iii) the Thomson effect [1], the evolution or absorption of heat when an electric current passes through a circuit composed of a single material that has a temperature difference along its length. The most common application of the Seebeck effect is the widely existing thermocouple, which can be used in thermometers, thermoelectric power generation, and other thermal cycle fields. Static cooling is the major application of the Peltier effect. The Thomson effect establishes a connection between the previous two and reflects their differential influence.
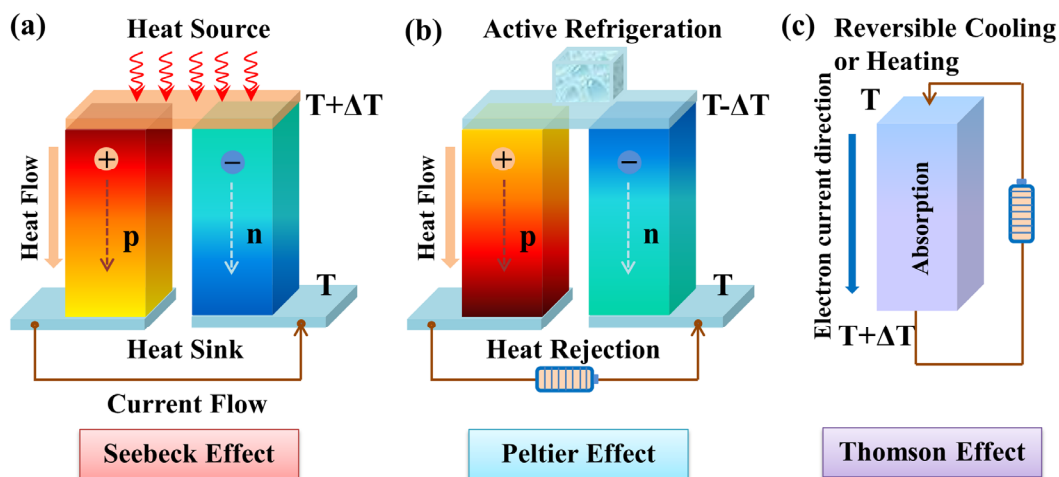
(a) Heat Source

(b) Active Refrigeration

(c) Reversible Cooling or Heating

Seebeck Effect

Peltier Effect

Thomson Effect

Figure 2. Schematic diagram of thermoelectric effects. (**a**) Seebeck effect for power generation, (**b**) Peltier effect for refrigeration, (**c**) Thomson effect for reversible cooling or heating.

The application of TEs is dependent on the assembled thermoelectric devices, with thermoelectric conversion efficiency serving as the most essential assessment metric. The thermoelectric power generation efficiency ϕ_{max} for the thermoelectric power system is [3]

$$\phi_{max} = \frac{T_C}{T_H - T_C} \frac{\sqrt{1 + (ZT)_{ave}} - T_H/T_C}{\sqrt{1 + (ZT)_{ave}} + 1} \tag{1}$$

For a thermoelectric refrigeration system, its maximum refrigeration efficiency η_{max} is [3]

$$\eta_{max} = \frac{T_H - T_C}{T_H} \frac{\sqrt{1 + (ZT)_{ave}} - 1}{\sqrt{1 + (ZT)_{ave}} + T_C/T_H} \tag{2}$$

where T_H and T_C represent the temperature of the hot and cold ends. It can be seen from formulas (1) and (2) that the first term is the efficiency of Carnot cycle power generation and refrigeration, respectively, while the second term is connected to the performance of TEs, and its value is smaller than 1. Therefore, the thermoelectric conversion efficiency is lower than the ideal Carnot cycle efficiency.

It can be found that the maximum thermoelectric conversion efficiency is a positive correlation to the average ZT value. To get a high ZT value, the material should have a large Seebeck coefficient, high electrical conductivity, and low thermal conductivity. First, briefly introduce the physical connotation of each parameter:

Seebeck coefficient (S): is often known as the thermopower defined by the Mott equation:

$$S = \frac{\pi^2}{3} \frac{k_B}{q} \kappa_B T \left(\frac{1}{n} \frac{dn(E)}{dE} + \frac{1}{\mu} \frac{d\mu(E)}{dE} \right)_{E=E_F} \tag{3}$$

where k_B is the Boltzmann constant, q is the electronic charge, T is the temperature, E_F is the Fermi energy, $n(E)$ is the carrier density at energy E, and $\mu(E)$ is the mobility at energy E [36]. It is evident that the S is inversely proportional to the carrier concentration, and the carrier concentration is also proportional to the effective mass of the carrier.

Electrical conductivity (σ) is a function of carrier concentration (n), carrier charge (e), and mobility (μ).

$$\sigma = ne\mu \tag{4}$$

Thermal conductivity (κ) refers to the inherent ability of materials to transmit or conduct heat, as electrons and phonons can carry heat energy, resulting in heat transfer

in solids. The total thermal conductivity consists of lattice thermal conductivity (κ_l) and electron thermal conductivity (κ_e), and it can be written as

$$\kappa = \kappa_e + \kappa_l \tag{5}$$

The Wiedemann-Franz formula can be used to calculate the electron thermal conductivity [36]:

$$\kappa_e = \sigma L T \tag{6}$$

where L is the Lorenz number in 10^{-8} W/(Ω K^2), which can be calculated using S by the equation of $L = 1.5 + \mathrm{Exp}\left[-\frac{|S|}{116}\right]$ [37]. Therefore, the κ_l is dominated in the thermal transport process in oxides TEs. The κ_l is closely related to phonon scattering, which is determined by the phonon mean free path (C_V), the average phonon group velocity (v_m), and specific heat at constant volume ($C_V = \rho C_p$, ρ is the bulk density of the sample, and C_p is the specific heat capacity at constant pressure) [38].

$$\kappa_{lat} = \frac{1}{3} C_V v_m l_p \tag{7}$$

Point defects, dislocations, grain boundaries, interfaces, and nano-sized second phases or inclusions are examples of scattering mechanisms that can be introduced into a microstructure to increase phonon scattering and thus decrease its κ over a wide temperature range. Thermoelectric materials with the ideal structure of "phonon-glass electronic-crystal" [39], such as the caged structure compounds and layered crystal structure components with "block modules", usually have low lattice thermal conductivity.

The ideal TE candidate would combine a large S, high σ, and low κ, yielding a high ZT value. However, the three parameters are closely coupled with each other, mutual restraint and mutual elimination; the improvement of thermoelectric performance needs to consider their complex relationship and make efforts to decouple them.

3. Fabrication of Thermoelectric Oxide Ceramics

3.1. Lattice Structures of Thermoelectric Oxide Ceramics

3.1.1. n-Type Thermoelectric Oxides

As an *n*-type thermoelectric oxide, strontium titanate (SrTiO$_3$) has attracted widespread interest due to its high effective mass of carriers, chemical and thermal stability at high temperatures, and high structural tolerance. SrTiO$_3$ has a cubic perovskite structure and Pm3m space group at room temperature, and its lattice constant is a = b = c = 3.905 Å [40]. Its crystal structure is shown in Figure 3a. In a unit cell unit connected by solid lines in the figure, Ti^{4+} ions occupy the central position in the unit cell, Sr^{2+} ions occupy the eight vertex positions, O^{2-} ions form an oxygen octahedron at the center of six faces of the cubic unit cell, and Ti^{4+} ions occupied the octahedral gaps. Therefore, the coordination number of Sr^{2+} ions is 12, and the coordination number of Ti^{4+} ions is 6. From another perspective, there is a cubic unit cell structure composed of eight Ti-O octahedrons in strontium titanate. Eight Ti-O octahedrons are located at the eight top corners of the cubic structure, while Sr^{2+} ions occupy the center of the cubic structure. The direct band gap of SrTiO$_3$ is 3.2 eV, and its σ is very low. Its phase transitions from cubic to tetragonal will occur at temperatures below 105 K [41].

As one of the *n*-type TEs, single crystal ZnO has a hexagonal wurtzite structure (a = 3.25 Å, c = 5.21 Å) [42,43]. Its crystal is shown in Figure 3b. ZnO has a broad band gap of 3.44 eV at 2 K. Zn 4s and O 2p states dominate its conduction and valence bands, respectively [43]. As the constituent elements (Zn and O) of zinc oxide have strong ionic bonds and light atomic mass, it has high lattice thermal conductivity $\kappa_l > 50$ Wm^{-1}K^{-1}, resulting in its poor ZT value < 0.01 [44,45].
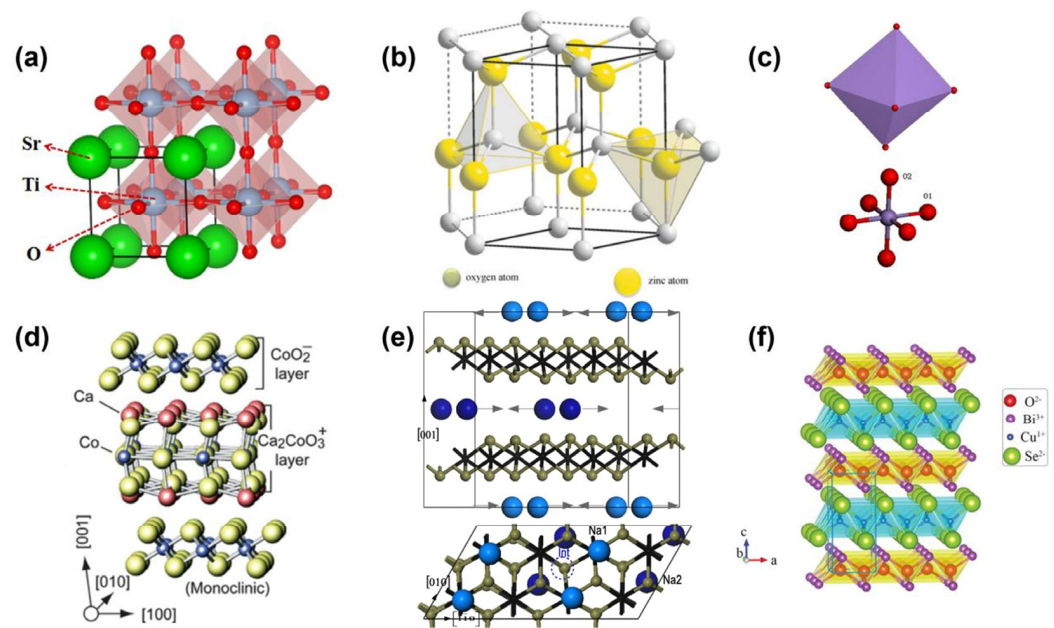
Figure 3. Schematic of the crystal structure of thermoelectric oxides. (**a**) SrTiO$_3$, (**b**) ZnO [43], (**c**) CaMnO$_3$ [29], (**d**) Ca$_3$Co$_4$O$_9$ [9], (**e**) Na$_x$CoO$_2$ [16], (**f**) BiCuSeO [21].

CaMnO$_3$ is an orthorhombic perovskite structure, and Mn^{4+}($t_{2g}^3 e_g^0$) occupies the center of the oxygen octahedron, as shown in Figure 3c [29,46]. The e_g^0 configuration enables pure CaMnO$_3$ to have insulating properties [28,47]. The theoretical indirect band gap of CaMnO$_3$ is ~0.7 eV. The Mn3d and Op states determine its electrical properties. According to the degree of hybridization, two kinds of oxygen, O1 and O2, exist. Because the degree of hybridization of Mn-O1 is higher than that of Mn-O2, carrier transport mainly occurs in the direction of Mn-O1. The formation of the O1 vacancy will hinder the conduction of carriers and reduce carrier mobility [29]. The existence of an O vacancy can cause partial Mn to transform from Mn^{4+} to Mn^{3+}, thus making the eg state of Mn partially occupied [47]. Mn^{3+} ions can exist stably in the system, and the material can be sintered in an air atmosphere at high temperatures. Therefore, its application environment does not need special atmosphere protection.

3.1.2. p-Type Thermoelectric Oxides

Ca$_3$Co$_4$O$_9$ is a typical representative material in *p*-type thermoelectric oxides. A rock salt type Ca$_2$CoO$_3$ layer sublattice and CdI 2 type CoO$_2$ slabs alternated arrangement into the layered structure of Ca$_3$Co$_4$O$_9$ [48,49]. Along the c-axis, it can be seen as a sandwich construction (rock salt plate sandwiched between two plates). Ca$_3$Co$_4$O$_9$ belongs to the monoclinic system structure, which is a C2/m superspace group. The incommensurate structure consists of two layers with distinct lattice parameters, a = 4.8323 Å, b1 = 2.82 Å, b2 = 4.55 Å, c = 10.8428 Å, β = 98.13°, allocated to 2.82 Å cells of CoO$_2$ subsystem (b1) and 4.55 Å cells of Ca$_2$CoO$_3$ subsystem (b2), as shown in Figure 3d [9]. Because the two sub-lattices have different b parameters, phonon scattering at the mismatched interfaces can contribute to hindering the heat transport properties [50].

Na$_x$CoO$_2$ is another potential layered cobalt-based thermoelectric material. As shown in Figure 3e [16], Na layers and CoO$_6$ octahedral layers with shared edges form the NaxCoO$_2$ lattice. In the sodium deficient system (x < 1), the Na ions show multiple configurations in its plane, reducing the crystal symmetry [17]. In addition, the high diffusivity of Na creates randomly distributed vacancies (as shown by the gray arrow in Figure 3e) at temperatures above the ambient temperature, so the highly disordered Na layer acts as a medium to interfere with phonon excitation propagation [18,19]. Therefore,

Na_xCoO_2 has a rather low thermal conductivity (0.01 $Wcm^{-1}K^{-1}$ at $T = 1000$ K) due to its dynamic and uncertain Na ion positioning.

BiCuSeO is a *p*-type oxide TE with excellent thermoelectric properties. It has a tetragonal crystal structure (a = b =3.9273 Å, c = 8.9293 Å, Z = 2) with symmetry of P4/nmm (No. 129) space group [20]. As depicted in Figure 3f, BiCuSeO possesses a layered "hybrid" crystal structure in which the conductive layer $(Cu_2Se_2)^{2-}$ alternates with the insulating layer $(Bi_2O_2)^{2+}$ [21,22]. The bond length of Bi-Se is 3.2 Å, which is larger than that of Bi-O of 2.33 Å, indicating that it has layer characteristics [20]. The $(Cu_2Se_2)^{2-}$ sublayer is the main conductive channel, called the conductive layer, which can be used to regulate electrical properties; the $(Bi_2O_2)^{2+}$ sublayer is a non-conductive layer (insulating layer), which can be effectively used for thermal conductivity suppression. Therefore, the layered structure of BiCuSeO-based compounds can achieve collaborative optimization of thermal and electrical conductivities.

There are still some thermoelectric oxides, such as $(Sr_xBa_{1-x})Nb_2O_6$ and $KSr_2Nb_5O_{15}$ with tungsten bronze crystal structure [51], $In_{2-2x}Zn_xCe_xO_3$ with body-centered cubic Bixbyite-type lattice structure and Ia3 (206) space group [33], and Magnèli phase of TiO_{2-x} [52], which showed relatively low *ZT* value and needed much more effort to improve their TE properties.

3.2. Preparation Method

3.2.1. Bulk Crystal Growth

It is reported that for *p*-type layered oxide TEs, the thermoelectric properties of single crystals are much higher than those of polycrystalline samples for a given component. For example, the figure merit *ZT* of single crystal Na_xCoO_2 and $Ca_3Co_4O_9$ samples reach 1.2 and 0.87, respectively, and the performance of polycrystalline samples is generally only about half of that of single crystal samples. The simple process of single-crystal preparation is shown in Figure 4a. Fujita et al. used the flux technique to prepare $Na_xCoO_{2-\delta}$ single crystals and measured their high-temperature thermoelectric properties for the first time. At 800 K, the *PF* reaches 7.7 $mWm^{-1}K^{-2}$, and the *ZT* value reaches 1.2 [53]. In 2003, Shikano et al. prepared a single crystal of $(Ca_2CoO_3)_{0.7}CoO_2$ using an enhanced strontium chloride flux method and measured its performance. At 973 K, the *ZT* value of $(Ca_2CoO_3)_{0.7}CoO_2$ single crystal reached 0.87 [54]. Although single-crystal oxide TEs have high thermoelectric properties, the costly preparation process of single crystal hinders its large-scale application. Thus, it is still important to develop and produce polycrystalline oxide TEs with superior performance.
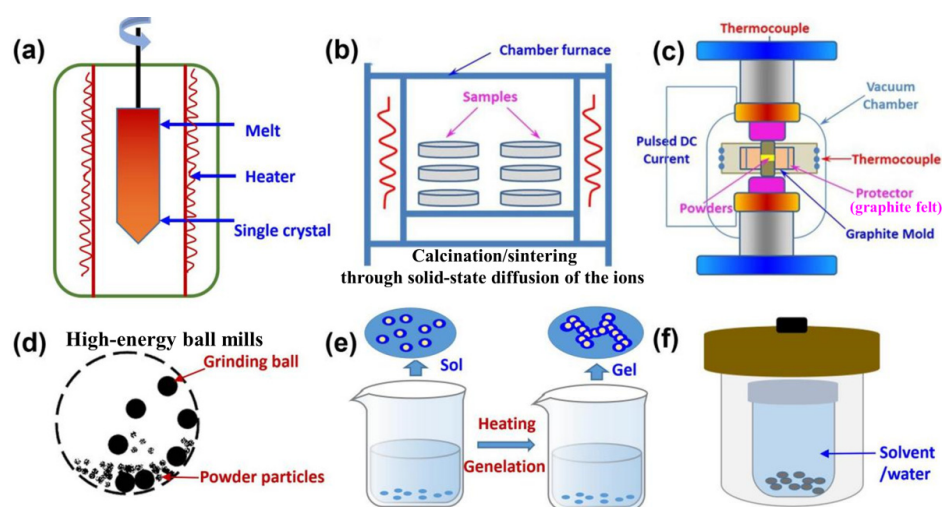

Figure 4. Diagram of synthesis method of oxide thermoelectric materials. (**a**) Bulk crystal growth, (**b**) solid-state method, (**c**) spark plasma sintering, (**d**) mechanical alloying, (**e**) colloidal synthesis, (**f**) hydrothermal/solvothermal synthesis.

3.2.2. Solid-State Method

The solid-state reaction method is the most widely employed method for preparing different oxide TEs [34,55–59]. Generally, two solid-state steps are required for the synthesis of polycrystalline oxide TEs, which mainly includes the preparation of pre-sintered powder, and then sintered compact bulk ceramic samples suitable for testing various properties, as depicted in Figure 4b. The high-purity solid precursor powders were mixed and calcined at high temperatures, such as TiO_2 and $SrCO_3$, required for the synthesis of strontium titanate [60]. This approach possesses the advantage of simplicity and low cost, but generally, the synthetic product after a high-temperature calcination process is blocky and requires a secondary ball milling to obtain fine powders to maintain high reactivity to sinter ceramics. For example, Qin et al. prepared different nano metal Ti additions of $Sr_{0.9}La_{0.1}TiO_3$ composite ceramics using the solid phase reaction technique. The nanoscale microstructure was controlled by adding nano metal powder and sintering aid of Bi_2O_3, and the high $ZT = 0.5$ of $SrTiO_3$-based components was obtained at 1073 K [23].

Adopting sintering aids is a commonly used method to improve the bulk density of ceramics in the traditional solid-state sintering process. The sintering aids have the following functions: (1) Forming a liquid phase environment and increasing the diffusion driving force of particles; (2) increasing ceramic density and controlling grain size; (3) preventing the polycrystalline transformation of the matrix material; and (4) entering into the lattice of the matrix material to form solid solutions during the later stage of sintering. At present, the common sintering aids include Bi_2O_3, CuO, V_2O_5, and B_2O_3, etc. [61–65].

Shi et al. prepared $(Ca_{0.85}Ag_{0.1}La_{0.05})_3Co_4O_9$ (CCO) ceramics by compositing the secondary phase Bi_2O_3 that can promote the densification to improve the bulk density, hence effectively improving the thermoelectric properties of CCO ceramics. According to the theory of liquid-phase sintering, when the sintering temperature exceeds 1097 K, Bi_2O_3 melts to form a liquid phase, and a dissolution–precipitation transport process occurs. The dissolved Bi_2O_3 promotes particle diffusion and sample densification and inhibits grain growth coarsening [66]. The difference in high-temperature solid-state reaction methods between BiCuSeO compounds and $SrTiO_3/Ca_3Co_4O_9$ is that since the raw powder contains metals Bi, Cu, and Se, it is necessary to vacuum the tank during ball milling to avoid oxidation. Additionally, the sintering also needs to be carried out in a vacuum quartz tube.

3.2.3. Spark Plasma Sintering

Spark plasma sintering (SPS) technology is also commonly utilized to prepare bulk oxide TEs [14,67–71]. SPS is also known as Pulse Electric Current Sintering (PECS). During the sintering process, the discharge plasma generated at the moment when the electrode is connected to the DC pulse current makes each particle inside the powder produce Joule heat uniformly and activate the particle surface, which makes it easy to prepare uniform, dense, and high-quality ceramic samples, as presented in Figure 4c. Furthermore, the sputtering and discharge impact of high-temperature plasma can remove impurities and adsorbed gas on the surface of powders, and the electric field can accelerate the diffusion process. Therefore, SPS has characteristics different from the traditional sintering method (the solid-state pressureless sintering process), that is, low sintering temperature and short sintering time, which can obtain fine and uniform grains and high-density materials [72]. The fine and uniform grains in the sample will suppress the thermal conductivity. Therefore, SPS is more suitable and efficient for preparing TEs than the traditional solid-state sintering method [73].

Ito et al. [74] prepared $Sr_{1-x}Y_xTiO_3/TiB_2$ composite ceramics by polymerization complexation process combined with SPS. The relative density of samples sintered at 1573 K for 5 min through the SPS method can reach about 99%, which is higher than that of samples sintered at 1673 K for 2 h by traditional hot-pressing sintering (97.2%). Reported experimental results confirmed that ceramics prepared by SPS technology could obtain fine-grain microstructure, and the thermal conductivity of the composite sample containing

TiB$_2$ remained lower than that of the hot-pressed ceramics [74]. In addition, to develop BiCuSeO oxyselenides TEs for industrial production on a large scale, Novitskii et al. [75] reported the process of batch synthesis of BiCuSeO by two-step reactive SPS method, which overcame the disadvantages of time-consuming, cumbersome, and energy consumption of solid-phase sintering technology.

3.2.4. Mechanical Alloying

Mechanical alloying is a method to obtain solid alloy or solid solution by high-speed ball milling or grinding, as shown in Figure 4d. Mechanical alloying has gained widespread attention for its advantages of a short cycle, low energy consumption, and simple process. Liu et al. studied the synthesis of La-doped SrTiO$_3$ nanopowders using mechanical alloying in an air atmosphere. In comparison to the solid-phase reaction method, the mechanical alloying technique can eliminate the calcination stage and is more cost-effective and eco-friendly [76]. Feng et al. prepared Bi$_{1-2x}$Ca$_x$Cu$_x$SeO samples by mechanical alloying [77], and the results show that these samples have high carrier concentrations. The maximum ZT = 1.15 was found for Bi$_{0.84}$Ca$_{0.08}$Pb$_{0.08}$CuSeO at 873 K as a result of the high concentration of Cu vacancies contributing to improving carrier concentration, refining grains, and decreased thermal conductivity.

3.2.5. Liquid-Phase Synthesis

(1) Colloidal Synthesis

Solid-phase reaction method has the disadvantages of low purity and high energy consumption. To overcome the shortcoming of the high-temperature solid-phase method, the hydrothermal synthesis and sol-gel method became aroused researchers' attention.

The materials synthesized by the sol-gel method generally use inorganic salt or organic alkoxide as the precursor and, through a chemical reaction such as hydrolysis polymerization, nucleation, and growth transform from liquid precursors to sol and then to a network structure known as a 'gel', and then after dried and heating treatment to obtain the target material, as illustrated in Figure 4e. For example, Michael et al. adopted the sol-gel technique to synthesize high-porosity Ca$_3$Co$_4$O$_9$ thermoelectric ceramics with a high ZT value of 0.4 [10]. In addition, the sol-gel approach also allows for the possibility of dispersing the cations used at the molecular level and the incorporation of dopants into the composition [11], which can be used as a dynamic, reliable, and environmentally friendly technique to develop novelty materials for potential TE applications.

(2) Hydrothermal Synthesis

The hydrothermal method is a solution reaction-based approach and can synthesize nanomaterials, which have been successfully applied for the preparation of TEs [78]. Usually, hydrothermal synthesis may occur over a wide temperature range from ambient temperature to extremely high temperatures and requires high-pressure conditions to generate high vapor pressures to trigger the chemical reaction or to control the morphology, as illustrated in Figure 4f. Compared to other preparation techniques, the products synthesized by the hydrothermal method present the advantages of controllable crystal size, homogeneous distribution, high efficiency, simple-to-manipulate stoichiometry, and ideal crystal morphology at lower temperatures. However, the products obtained by hydrothermal synthesis need to be separated, washed, and dried [79,80]. Wang et al. successfully synthesized Nb-La co-doped SrTiO$_3$ nanopowders using the hydrothermal technique and bulk ceramics with a complex micro and electron structure arising from the nano-inclusions and the second phases precipitated from the matrix were obtained with high-level ZTs >0.6 at 1000–1100 K [36].

(3) Solvothermal Synthesis

As illustrated in Figure 4f, the solvothermal synthesis is analogous to the hydrothermal method and is based on heating the precursors and a solvent in a closed system at a temperature above the boiling point of the solvent used [60]. The synthetic procedure usually

requires high temperature and high pressure to create the supercritical circumstances to develop the peculiar behavior of the solvent, exerting different influences on the precursors resulting in the desired product. Park et al. synthesized Ag-SrTiO$_3$ nanocomposites by one-pot solvothermal method [81] using strontium nitrate (Sr(NO$_3$)$_2$), silver (I) nitrate (AgNO$_3$), and titanium tetraisopropoxide [(CH$_3$)$_2$CHO]$_4$Ti (TTIP) as starting ingredients. Furthermore, the loading quantity of Ag could be easily manipulated by adjusting the concentration of the AgNO$_3$ precursor. In addition, the thermoelectric properties of layered TEs can be effectively controlled by bottom-up wet chemical synthesis of two-dimensional nanosheets/nanoplates [82–84]. Samanta et al. used Cu(NO$_3$)$_2$·3H$_2$O, Bi(NO$_3$)$_2$·5H$_2$O, and selenourea as raw materials, and in the presence of KOH/NaOH, prepared multilayer ultra-thin BiCuSeO nanosheets by low-temperature solvothermal method [85] and the obtained nanosheet samples showed lower lattice thermal conductivity and better electron transport properties than that of the bulk samples.

In addition to the preparation methods listed above, there are also some other techniques, such as hot-pressing sintering, 3D printing technologies, direct ink writing, etc., that can also be used in the TE fields for material research and development.

4. Development and Strategies to Improve the Thermoelectric Performance of Oxide Ceramics

Several of the selection rules are somewhat paradoxical as a result of the inherent trade-off effect between σ and S. Many optimized strategies may have a complicated correlated impact on S, σ, and κ. As an illustration, the increase of doping concentration will improve σ while decreasing S. Then, Ioffe's finding in doped semiconductors was the first effort to empirically determine the carrier concentration "sweet spot" of excellent thermoelectrics is $n = 10^{18}$–10^{20} cm^{-3} [86]. Consequently, an optimal power factor ($PF = S^2\sigma$) versus doping concentration exists at a relatively high doping level. Furthermore, a further decrease of κ is necessary to produce a high ZT.

The content of this section is convenient for sorting out and summarizing the development and optimization strategies of band engineering, doping, entropy engineering, defect engineering, grain boundaries, texture, composites, etc. Development is still in progress, and researchers are devoted to searching for new TEs and novel optimization strategies to enhance their performance and accelerate their applications.

4.1. Band Engineering

Since S, σ, and κ of TEs are determined by the transport and interaction of carriers and phonons, adjusting one parameter often may sacrifice other physical parameters, making achieving collaborative optimization of thermoelectric performance a huge challenge. In bulk TEs, the band gap, the degeneracy of the conduction band, the extreme value of the valence band, and the effective mass in the band structure are fundamental parameters that determine the thermoelectric performance. According to the Mott formula [36], the parameter of S is in direct proportion to the slope of the energy band near the Fermi level. A greater slope means a greater S. Furthermore, the S is a function of the variation of σ near the Fermi surface, and increasing the complexity of the crystal structure can increase the complexity and the degeneracy of the band structure, leading to more extreme values in the conduction band and valence band, thus increasing S. In a word, factors of the band gap, energy band shape, effective mass of carriers, mobility, etc., determined by band structure are closely related and produce a trade-off effect on thermoelectric performance. At present, the energy band engineering strategy mainly includes multi-valley degeneracy, energy band converges, resonance energy level, energy filtering, and modulating doping.

Moreover, complex band structures with high degeneracy numbers can exist because of the relatively high symmetry in perovskite structures such as SrTiO$_3$. Due to the correlation between energy band characteristics (such as DOS and band convergence) and carrier transport properties, the electrical properties can be optimized through energy band engineering. As widely observed in BiCuSeO [87], effective mass m^* gradually decreases as the carrier concentration decreases, indicating band nonparabolicity. Results of calculations

suggest that a bigger m^* in $SrTiO_3$ can lead to a greater DOS of the triply degenerate $3d$-t2g orbitals near the conduction band bottom, which contributes to a larger $|S|$ and a higher $S^2\sigma$ [88]. Figure 5 shows the calculated band structures and DOS of pristine $SrTiO_3$, $Sr_{0.9}La_{0.1}TiO_3$, and $Sr_{0.9}La_{0.1}Ag_{0.1}Bi_{0.1}TiO_3$ samples [88], respectively. In addition, the ab initio Molecular Dynamics and DFT simulations results [89,90] demonstrated the softening of the c-axis polar mode, and the shift in the dispersion of the acoustic bands could decrease the thermal conductivity. It was notable that another crucial feature of the band structure is the density-of-states effective mass (m^*), which is closely related to carrier mobility (μ). Usually, the *PF* is positively proportional to the weighted mobility of $\mu\left(\frac{m^*}{m_e}\right)^{\frac{3}{2}}$, where m_e is the free-electron mass. Hence, it is preferable to maximize both m^* and μ; large m^* corresponds to large *S*, and big μ promotes the electrical conductivity. Nevertheless, this is difficult in practice, and heavy carriers are less mobile ($\mu = e\tau/m^*$); hence the trade-off arises.
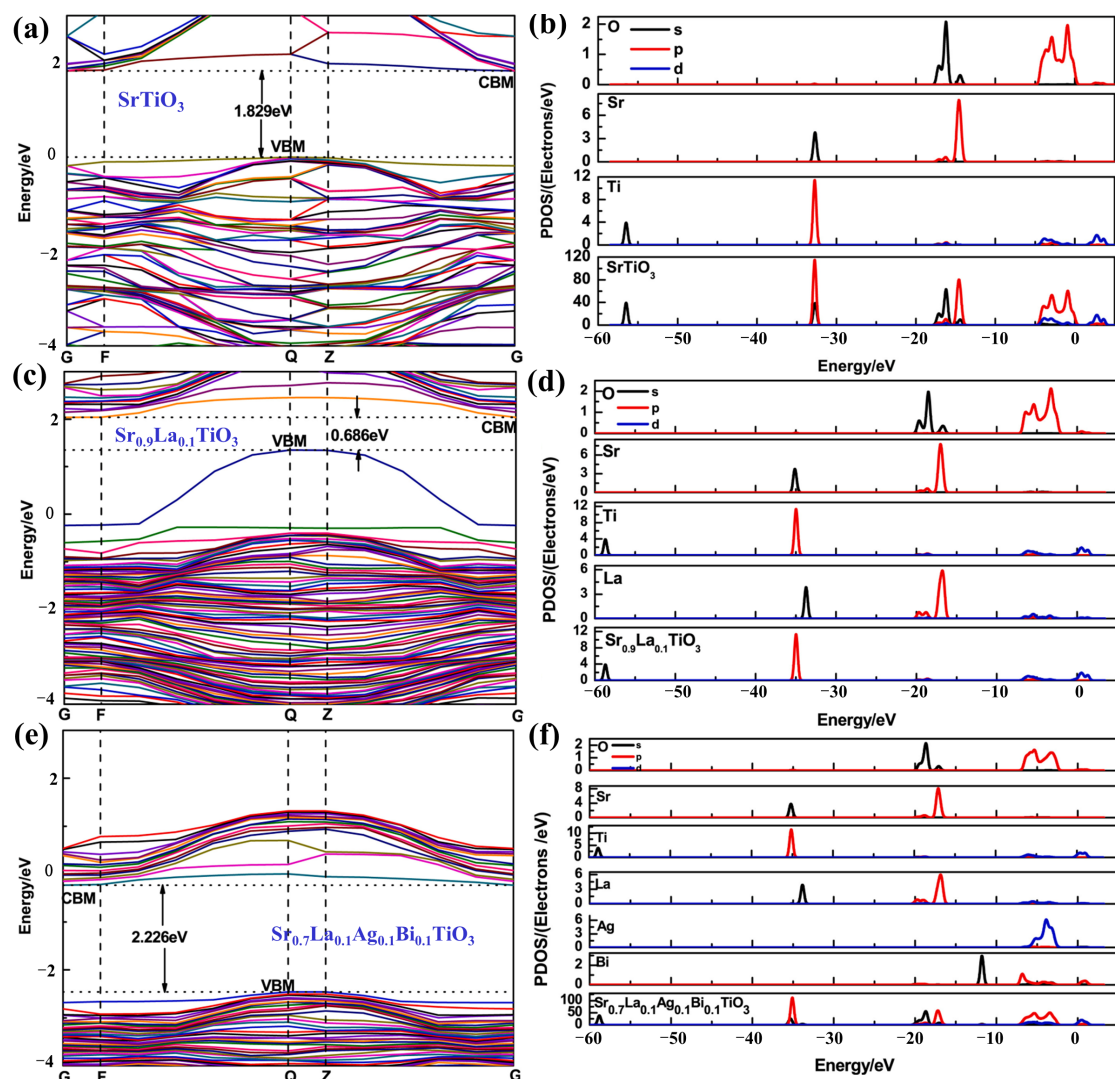

Figure 5. Calculated band structures and PDOS of (**a**,**b**) pristine $SrTiO_3$, (**c**,**d**) $Sr_{0.9}La_{0.1}TiO_3$, and (**e**,**f**) $Sr_{0.7}La_{0.1}Ag_{0.1}Bi_{0.1}TiO_3$ [88].

In addition, alloying with suitable elements can introduce some resonant states resulting in highly anisotropic and multiple valence bands for achieving the desired band structure. It should be emphasized that the aforementioned basic rules for optimum band structure and thermoelectric properties are only applicable to homogeneous single-phase

semiconductors. In the case of composite TEs (such as those incorporated with nanoscale inclusions), which will be discussed later, many of the trade-offs discussed above can be suppressed or even overcome.

4.2. Doping

Element doping is one of the widely used basic strategies to regulate carrier concentration for enhancing the thermoelectric performance of TEs. By properly doping elements with different valence states into different cationic lattice sites, a well-regulated n can be obtained, which leads to an optimized $S^2\sigma$. Doping will cause a change in cell parameters, induce point defects, and bring lattice distortion because of the position of atoms and the length of valence bonds changed, resulting in variations of S, κ, and σ. Furthermore, the length and strength of the valence bond is an important parameter that determines thermal conductivity.

In n-type $SrTiO_3$-based TEs, trivalent states of La [23,25,36,65,67,76,78,91], Ce [91], Nd [91], Sm [91,92], Gd [91], Dy [91], Pr [93], and Y [74] can be used to dope in Sr^{2+} site. The valence states of $\geq 5^+$, such as Ta [94], Nb [24], and W [95], can be used to dope in the Ti^{4+} site. K. Singsoog et al. [96] investigated the influence of La doping amount on $Sr_{1-x}La_xTiO_3$ (x = 0, 0.06, 0.13, 0.25) through theoretical calculation; the results show that the parameters (S, σ, κ, PF, and ZT) increase first and then decrease. When the doping concentration of La = 0.13, it has the best thermoelectric performance of $S_{900K} = -450$ μ V/K, $PF_{1200K} = 2.55$ mW/m/K^2. Figure 6a shows the reported results of substituting Sr with rare earth elements of La, Nb, Sm, Gd, and Dy in $SrTiO_3$. Results demonstrate that the large ion radius of the doped element (such as La, Nb, Sm) is advantageous to raise the power factor, and the small ion radius of doped elements (such as Gd, Dy, Er, Y) can effectively reduce the thermal conductivity [91]. Besides the above single-doping on the A/B site of ABO_3, co-doping on both Sr and Ti-site is also widely employed, such as $Sr_{0.8}La_{0.18}Yb_{0.02}TiO_3$ with a $ZT = 0.31$ at 1023 K [97], and $Sr_{0.87}Dy_{0.07}Nd_{0.06}TiO_3$ with a $ZT = 0.19$ at 673 K [98]. Figure 6b shows high $ZTs > 0.6$ were obtained at 1000–1100 K in La-Nb co-doped $SrTiO_3$ [36] through nano-scale modification and microstructure regulation strategies which are at a high-performance level.

In the n-type $CaMnO_3$ system, three types of elements doped at the Ca position are rare earth elements (La, Y, Ce, Sm, Pu, Nd, Lu, etc.) [99,100], main group elements such as Bi [101] and alkaline earth elements (Ba, Sr, Mg, etc.) [102]. Additionally, the doped elements in the Mn site mainly include Ta, V, Nb, Ru, etc. [103]. The doping cases such as $Ca_{1-x}Bi_xMnO_3$ ($0 \leq x \leq 0.10$) [101], $CaMn_{1-x}Nb_xO_3$ (x = 0.02, 0.05, 0.08) [104], Dy and Yb co-doping on $Ca_{1-2x}Dy_xYb_xMnO_3$ ($0 \leq x \leq 0.10$) [105], and $Ca_{0.92-x}Pr_{0.08}Sr_xMnO_3$ (x = 0.01, 0.02, 0.03, 0.04) [106] demonstrated that Bi, Nb, Dy, Yb, Pr doping at $CaMnO_3$ obtained the ZT values range of 0.18–0.27 which were much improved compared with the pure phase of $CaMnO_3$ ($ZT = 0.04$).

To improve the thermoelectric properties of ZnO, commonly used doping elements are C, Si, Fe, In, Ga, Al, Ni, and Sb [34,107–109]. Among them, Al-doped ZnO is the one widely studied and has the best TE performance at present. In the case of $Zn_{0.96}Al_{0.02}Ga_{0.02}O$ [107], $ZT = 0.65$ at 1247 K was obtained, which is one of the high levels of ZT values in n-type oxide thermoelectric materials. Additionally, this outstanding achievement can be attributed to the Al and Ga co-doping can significantly reduce the thermal conductivity from 40 W/m/K of $Zn_{0.98}Al_{0.02}O$ to 5 W/m/K of $Zn_{0.93}Al_{0.02}Ga_{0.05}O$.

In the p-type $Ca_3Co_4O_9$-based TEs, much research focused on the partial substitution of cations on the Ca-site such as Na [110], Sr [111], Ba [112], La [12], Ag [12], Fe [113], Pb [114], Ag [115], Ga [116], Tb [117], and Yb [118], while Ni [119], Mn [120], Cu [120], and Ir [121] were introduced into the Co-site to optimize the thermoelectric properties in the $Ca_3Co_4O_9$ system. Specifically, as R^{3+} has a higher oxidation state than the Ca-site, it may decrease the carrier concentration to improve the Seebeck coefficient.
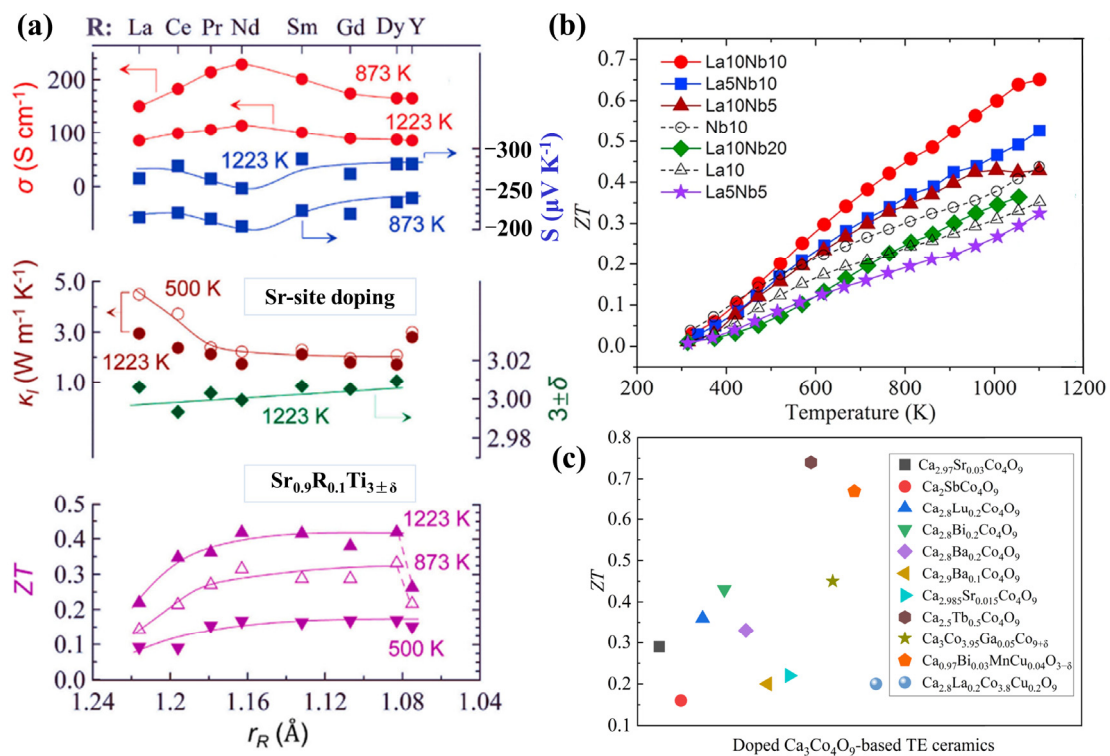
Figure 6. (**a**) Thermoelectric parameters (σ, S, κ_1, $3 \pm \delta$, and ZT) of polycrystalline $Sr_{0.9}R_{0.1}TiO_{3\pm\delta}$ sample, "R" represents a different rare-earth element with various ionic radii (r_R) as shown in the *x*-axis [91], (**b**) ZT values of the La and Nb co-doped $SrTiO_3$ [36], (**c**) ZT values of the doped $Ca_3Co_4O_9$ system [111–123].

Figure 6c summarizes ZT values of typical element doping in the $Ca_3Co_4O_9$ system. Specifically, Tb-doped $Ca_3Co_4O_9$ [117], La and Co co-doped ceramic of $Ca_{2.8}La_{0.2}Co_{3.8}Cu_{0.2}O_9$ [122], Ag and Fe co-doped system of $Ca_{2.95}Ag_{0.05}Co_{3.8}Fe_{0.2}O_9$ [123] obtained ZT values of 0.16–0.74 attaining the collaborative optimization of electron and phonon transport. In addition, these results demonstrate that a suitable quantity of Ag and Fe co-doping can significantly boost σ arising from higher n and μ while decreasing κ due to the enhanced phonon scattering.

For Na_xCoO_2-based TEs, the adjustable space of their thermoelectric properties is greater than that of the $Ca_3Co_4O_9$ system, mainly because the content of Na^+ ions has a great influence on the conductivity. Substitution at either the Na site (with K, Sr, Nd, Sm, Yb, Mg, etc.) [51,124] or the Co site (with Ag, Pb, Mn, Ru, Pd, etc.) [125–128] of $NaCoO_2$ allows for fine-tuning of its carrier concentration, magnetic ordering, and phonon frequency. Since $NaCoO_2$ is a tightly correlated electron system, Co-site substitution can alter the magnetic and TE characteristics. In the Cu, Y, Sn, W, Au, and Bi-doped Na_xCoO_2 system [16], when the dopant is situated in the Na layer of the Na_xCoO_2 lattice structure, the maximum thermoelectric performance is reached and confirmed by the DFT simulation results. The improved ZT values can be ascribed to the beneficial effect of boosting carrier mobility being greater than the negative impact of decreasing the carrier concentration of holes on the electrical conductivity of these dopants. A record-high $ZT = 1.24$ was achieved at 1010 K in single-phase Na-doped Na_xCoO_2 (x = 1, 0.98, 0.96, and 0.94) ceramics [129].

Compared with other *p*-type oxide TEs, κ of BiCuSeO is very low (0.4~0.7 W/m/K) [21,22], originating from its strong crystal anharmonicity [130]. At present, an extremely low $\kappa = 0.33\ Wm^{-1}K^{-1}$ at 300 K was achieved in heavily doped $Bi_{0.875}Ba_{0.125}CuSeO$ alloys [130]. After doping, the electrical conductivity of BiCuSeO can be further increased and thus improve ZT values. For example, the maximum $ZT = 1.5$ of $Bi_{0.88}Ca_{0.06}Pb_{0.06}CuSeO$ was obtained [21], which is three times of pure BiCuSeO.

In the In_2O_3 system, the $ZT = 0.47$ at 1223 K was reached for the $In_{1.92}Ce_{0.08}O_3$ sample [131] through a synergistic effect of secondary CeO_2 nanoclusters and fine grain size, which can contribute to greatly lowering the thermal conductivity. Furthermore, in the heavily doped nanostructured In_2O_3-based ceramics [33,132], the increased σ and decreased κ can be achieved simultaneously. The remarkable result is κ_l decreased by 60%, and the minimum value is 1.2 W m^{-1} K^{-1} at 973 K, which is close to the amorphous limit, and finally, the highest $ZT = 0.44$ at 973 K.

It is worth mentioning that in the porous Gallium-doped In_2O_3 [133], an extremely low $\kappa = 0.21$ W m^{-1}K^{-1} at ambient temperature and a high $ZT = 0.38$ at 800 °C was achieved through the pore structure regulation combined with doping strategy.

4.3. Entropy Engineering

Due to its superior characteristics, such as low thermal conductivity [59,61,134–136], high-entropy ceramics (HECs) containing five or more cations have lately gained considerable interest in the TE field. High-entropy engineering has been confirmed to increase the S and reduce the κ_l in TE oxide ceramics, making it a promising strategy for optimizing thermoelectric performance by broadening the composition design. High-throughput screening has been used to construct multi-component TEs with high entropy, as reported by Zhang et al. [137] and Liu et al. [138]. By decreasing the κ_l and/or increasing S, high-entropy engineering can become an efficient technique to considerably improve thermoelectric performance. Figure 7a–c shows Zhang et al.'s work of high-entropy $(Ca_{0.2}Sr_{0.2}Ba_{0.2}La_{0.2}Pb_{0.2})TiO_3$ ceramics with perovskite structure, which presented a relatively high $|S| = 272$ µV/K and ultra-low $\kappa = 1.75$ W/m·K at 1073 K [59] because of the short-range disordered distribution characteristic of the A-site cations. In Zheng et al.'s work of $(Ca_{0.2}Sr_{0.2}Ba_{0.2}La_{0.2}Pb_{0.2})TiO_3$ ceramics [139], the minimum $\kappa = 1.17$ W/(m·K) at 923 K and the maximum $ZT = 0.2$ at 873 K was obtained. Lou et al.'s work reported that the B-site multi-components of $Sr_{0.9}La_{0.1}(Zr_{0.25}Sn_{0.25}Ti_{0.25}Hf_{0.25})O_3$ exhibit low $\kappa = 1.89$ W/(m·K) and a high S = 393 µV/K) [61] at the same time. Researchers focus on not only the five-component high-entropy TE oxide ceramics but also the four-component system of $(Sr_{0.25}Ca_{0.25}Ba_{0.25}RE_{0.25})TiO_3$ (RE = La, Ce, Nd, Sm, Eu) that were designed and synthesized by solid-state reaction route [134,135]. Significantly, the $(Sr_{0.25}Ca_{0.25}Ba_{0.25}RE_{0.25})TiO_3$ sample exhibited the temperature-independent variation characteristics of κ_l ranging from 2.31 to 2.27 W/(m·K) over 373 K-1073 K testing temperature range which is analogous to the characteristic of glass with a constant phonon mean free path (l_{ph}). As predicted by the Debye-Callaway model, an ultralow $\kappa = 0.7$ W/mK at 1100 K was obtained in the *n*-type high-entropy perovskites $Sr(Ti_{0.2}Fe_{0.2}Mo_{0.2}Nb_{0.2}Cr_{0.2})O_3$ [140] through the increased electron-phonon and Umklapp scattering. A series of high-entropy $(RE_{0.2}Ca_{0.2}Sr_{0.2}Ba_{0.2}Y_{0.2})MnO_3$(RE = La^{3+}, Nd^{3+}, Ho^{3+}, Lu^{3+}) ceramics were prepared and the low $\kappa = 0.94$ W/(m·K) at 800 °C was found for the $(Lu_{0.2}Ca_{0.2}Sr_{0.2}Ba_{0.2}Y_{0.2})MnO_3$ sample [141].

In contrast to the usual observed in non-high-entropy $SrTiO_3$-based TEs, κ sharply dropped from ~7.16 W/(m·K) to ~2.89 W/(m·K) over 300 K–1073 K. Figure 7d–i shows the temperature-independence κ over the testing temperature range of 323 K-1073 K [134,135] realizing 'phonon-glass electron crystal' (PGEC) and with the minimum $\kappa = 2.27$ W/(m·K) for the 4Ho sample.

However, carrier mobility can be deteriorated to hinder electron transport due to high configuration entropy, which also leads to poor electrical conductivity. Consequently, future work devoted to pursuing high ZT values should concentrate on multiple types of strategies that cooperate in optimizing σ, particularly in improving the carrier mobility meanwhile maintaining the obtained ultra-low intrinsic κ_l for advancing the industrialization of TE oxides at high temperatures.
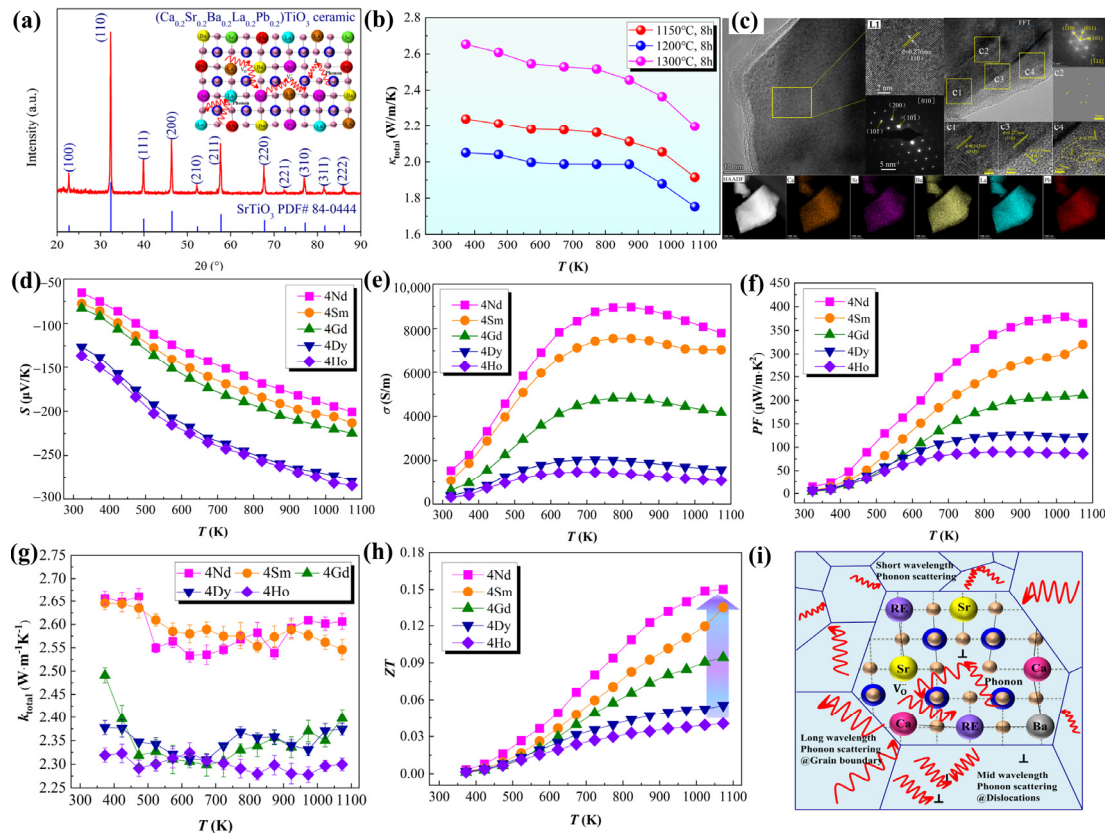
Figure 7. (**a**) XRD patterns, (**b**) κ, (**c**) TEM results of the high-entropy $(Ca_{0.2}Sr_{0.2}Ba_{0.2}La_{0.2}Pb_{0.2})TiO_3$ ceramics [59]. (**d**–**h**) S, σ, PF, κ_{total}, and ZT values of the high-entropy $(Sr_{0.2}Ca_{0.255}Ba_{0.25}RE_{0.25})TiO_3$ ceramics [134]. (**i**) Schematic diagram of the possible phonon scattering in reducing lattice thermal conductivity for high-entropy ceramic [135].

4.4. Defect Engineering

In ionic compounds, the heat transport mechanism is dominated by κ_l. Additionally, κ_l can be lowered due to phonon scattering. Based on Debye–Callaway's model and the relaxation-time approximation, the κ is a function of phonon scattering rates ($1/\tau$) or the relaxation time (τ) [142]. τ has contributions from grain boundary scattering (τ_B), point defect scattering (τ_{PD}), phonon-phonon Umklapp scattering (τ_U), and electron-phonon scattering (τ_{ep}) as represented by Equation (8) [142,143].

$$\frac{1}{\tau} = \frac{1}{\tau_B} + \frac{1}{\tau_{PD}} + \frac{1}{\tau_U} + \frac{1}{\tau_{ep}}$$

$$= \frac{v_m}{L} + A\omega^4 + B\omega^2 T exp\left(\frac{-\Theta_D}{nT}\right) + C\omega^2 \qquad (8)$$

Here, v_m is the mean acoustic velocity, L is the average grain size, Θ_D is the Debye temperature, ω is the phonon frequency, and A, B, and C are parameters corresponding to the point defects, Umklapp process, and electron-phonon scattering, respectively. Phonons are more likely to be strongly scattered by lattice defects of considerable size. Therefore, during the defect regulation, attention should be paid to building a full-scale hierarchical structure containing defects of various forms and scales to achieve "total phonon scattering" in a broad frequency range. Specifically, the atomic scale point defects, such as vacancy, replacement atoms, etc., can realize effective phonon scattering by the high-frequency short wavelength [134,136]. Nanoscale defects such as dislocations and nano precipitates can achieve effective scattering of phonons with a moderate mean free path. Mesoscopic scale (micrometer level) features such as grain boundaries, phase interfaces, pores, clusters, etc.,

can realize the effective scattering of large free path phonons. Based on this full-scale hierarchical structure, it can achieve enhanced phonon scattering and obtain low lattice thermal conductivity.

Controlling the A-site deficiency [27,54,144,145] and oxygen vacancies [27,146] in the donor-doped $SrTiO_3$ ceramics can create mobile carriers to improve their thermoelectric performance. By mixed-donor doping, a high concentration of the A-site vacancies was created, which can combine with the oxygen vacancies to form Schottky pairs. For example, in the $Sr_{0.825}La_{0.05}Ce_{0.05}Ti_{0.95}Nb_{0.05}O_3$ sample [27], a large Sr deficiency was created with the help of liquid-phase sintering, leading to abundant Sr-O vacancy pairs formed as electronic defects without compromising carrier transport across the grain boundaries, which results in the *ZT* value surpass 0.38 at 1000 K. Kovalevsky et al. [54,91] explored and clarified the links and interactions of defect engineering combined with co-substitutional doping with La. The combined effect of A-site vacancies, oxygen vacancies, and the generated Ti^{3+} contribute to *ZT* values up to 0.42 under highly reducing sintering conditions [91].

In summary, defects engineering of the introduction of A-site cation vacancies such as $Sr_{1\pm y}Ti_{0.9}Nb_{0.1}O_{3\pm\delta}$ [55] and $Sr_{0.95}Sm_{0.0125}Dy_{0.0125}Ti_{0.90}Nb_{0.10}O_{3\pm\delta}$ system [147], or oxygen vacancies of $Sr_{0.8}La_{0.067}Ti_{0.8}Nb_{0.2}O_{3-\delta}$ [144], play a synergistic role in charge and phonon transport properties specifically generating additional phonon scattering centers including point defects, dislocations, and strain fields to suppress κ while maintaining rapid carrier transport in the perovskite lattice; hence, the resulting *ZT* ranges in 0.25–0.4.

In the $CaMnO_3$ system, single doping of Fe^{2+} and Al^{3+} on the Mn site or dual doping of Ni-Fe and Al-Ga on the Mn site [102] can facilitate the formation of O vacancies. The oxygen vacancies order in a zig-zag arrangement in partial reduction $CaMnO_{2.75}$ can improve *S*, and a brownmillerite-like structure is expected to form in a further reduction to $CaMnO_{2.5}$ according to first-principles calculations.

In the BiCuSeO system, an effective strategy to realize the collaborative optimization of thermoelectric property through Bi/Cu dual vacancies reached a high *ZT* = 0.84 at 750 K [148]. Moreover, positron annihilation spectroscopy shown in Figure 8a combined with a Schematic representation of trapped positrons (Figure 8b) confirms the interlayer charge transport between these Bi/Cu dual vacancies, which results in a notable improvement in σ maintaining a relatively high *S* to realize the synergistic effect of enhancing phonons scattering without deteriorating the electrical transport properties (Figure 8c,d). Figure 8 shows the ultra-low κ = 0.37 W m^{-1} K^{-1} at 750 K obtained as a result of the dual vacancies introduced compared to the pristine and monovacancy samples.
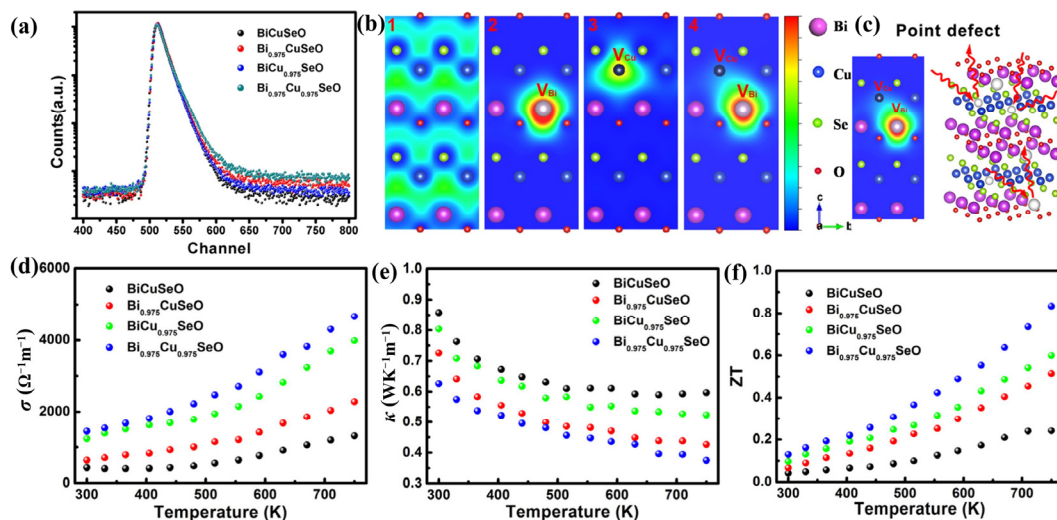

Figure 8. (**a**) Positron lifetime spectrum. (**b**) Schematic representation of trapped positrons for $Bi_{1-x}Cu_{1-y}SeO$ samples in (100) plane. (**c**) Schematic representation of phonon scattering with Bi/Cu vacancies. (**d–f**) σ, κ, and *ZT* values of the $Bi_{1-x}Cu_{1-y}SeO$ samples [148].

Dislocations in the lattice can dramatically increase phonon scattering to suppress the lattice's thermal conductivity while maintaining high carrier transport. Due to phonon scattering on dislocation cores ($\tau_{DC} \propto \omega^{-3}$) and dislocation strain fields ($\tau_{DS} \propto \omega^{-1}$) exhibiting frequency dependency properties, dislocation is especially effective for scattering mid-range frequencies phonons. In oxide TEs, creating a high density of dislocations can be accomplished by introducing a large concentration of vacancies. In the reduction annealing process of $SrTiO_3$-based TEs, these vacancies diffuse to create lower energy vacancy clusters, which then collapse into edge dislocations. In the HRTEM images (Figure 9) of high-entropy $(Ca_{0.2}Sr_{0.2}Ba_{0.2}La_{0.2}Pb_{0.2})TiO_3$, $Sr_{0.9}La_{0.1}(Zr_{0.25}Sn_{0.25}Ti_{0.25}Hf_{0.25})O_3$, $(Sr_{0.25}Ca_{0.25}Ba_{0.25}La_{0.25})TiO_3$, and $(Sr_{0.25}Ca_{0.25}Ba_{0.25}Nd_{0.25})TiO_3$ system [59,61,134,135], edge dislocations are detected, and the corresponding strain field distribution is quantified by geometric phase analysis (GPA, presented in Figure 9c3).
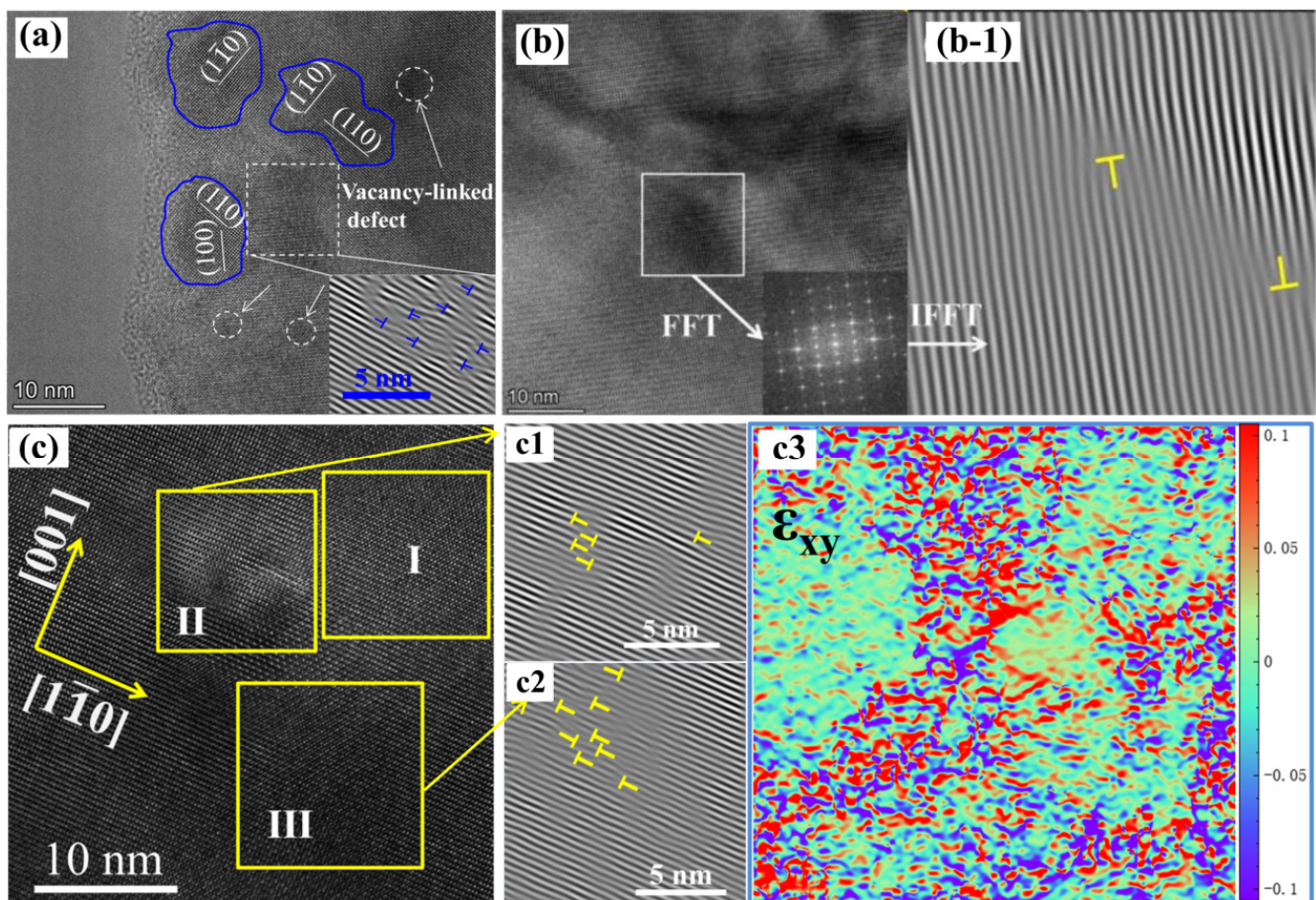

Figure 9. (**a**) HRTEM images of the $(Sr_{0.25}Ca_{0.25}Ba_{0.25}RE_{0.25})TiO_3$ sample [135], (**b**) HRTEM images and the corresponding FFT image and IFFT image (**b-1**) along the [100] zone axis of the $Sr_{0.9}La_{0.1}(Zr_{0.25}Sn_{0.25}Ti_{0.25}Hf_{0.25})O_3$ sample [61], (**c**) HRTEM images and the corresponding IFFT images (**c1,c2**) and strain map (**c3**) by geometric phase analysis (GPA) method [134].

In addition, collision with the "cage" can result in greater chemical bond anharmonicity, resulting in resonant phonon scattering of the "Rattle type". For example, the $Na_{0.8}CoO_2$ sample [149] has a large-period superstructure with multiple vacancy clusters existing throughout a broad concentration range that are also responsible for rattling modes confirmed by the inelastic X-ray and neutron scattering techniques. At low energy, the Einstein-like rattling mode is correlated to large anharmonic shifts of Na^+ in multi-vacancy clusters has been directly observed. Correspondingly, κ is reduced by a factor of six due to these rattling modes compared to that of vacancy-free $NaCoO_2$. Compared with conven-

tional defect scattering, this scattering mode has more simple phonon selectivity, higher scattering frequency, and greater scattering intensity, which can cause strong dispersion of phonons at specific frequencies (mainly low frequencies).

Due to the defects can also act as the potential scattering center of the electron. One key point to note in "defect engineering" is that the positive effect of reduction in κ can compensate for even surpassing the negative impact on electrical conductivity decrease. Therefore, defect engineering involving defects concentration, microstructure characteristics, and their distribution should be in a rational range of importance for improving thermoelectric performance.

4.5. Grain Boundary and Nanostructure Engineering

Grain boundaries (GBs) form ubiquitous microstructures in polycrystalline oxide ceramics, which play a significant role in tuning their *ZT*. Different grain size has a varied impact on σ and κ. To ensure that the effect of GBs or/and the nanostructure on decreasing κ is larger than its deterioration in σ, the grain sizes should be appropriately tuned. The energy filtering mechanism was proposed, meaning that randomly distributed potential barriers can filter away low-energy carriers to cause a decrease in the actual carrier density to improve *S*. In the nanostructured polycrystalline ceramic TEs, low energy carrier filtering effects combined with the enhanced phonon scattering can effectively suppress κ_l [26,65,78,150,151], confirmed by both computational and experimental results.

Optimized thermoelectric performance by grain boundary and nanostructure are mainly reflected in lowering κ [78,152], or the formation of a conductive path at grain boundary to promote the carrier mobility; these two factors play a synergistic effect on the electron and phonon transport process contribute to a trade-off *ZT* values of 0.3–0.4. In the cases of the nanostructured $Sr_{0.91}La_{0.09}TiO_3$ sample, *ZT* = 0.37 was achieved at 973 K [153], a greatly improved performance *ZT* = 0.35 in Pr-doped of $SrTiO_{3-\delta}$ because of the Pr-rich grain boundaries contributed to improving carrier mobility [153,154], and the improving *ZT* = 0.38 obtained in $Sr_{0.8}La_{0.067}Ti_{0.8}Nb_{0.2}O_{3-\delta}$ system containing Cu or Fe inclusions [155]. Figure 10a–f presents the nano-scale powder and $Sr_{0.9}La_{0.9}Ti_{0.9}Nb_{0.9}O_3$ bulk ceramic which exhibit high electrical conductivity and *PF* through the synergy effect of modulation doping and microstructure controlling approach.

Due to enhanced boundary scattering, a low κ = 3 W/m K at room temperature was obtained in bulk ZnO [34] with a grain size of 20 nm prepared by the pulsed electric current sintering method under a pressure of 500 MPa. The nanostructured $CaMn_{0.98}Nb_{0.02}O_3$ [83] was synthesized by ultrasonic spray combustion (USC) method with κ decreasing from ~2.5 W m^{-1} K^{-1} at 300 K to less than 1.5 W m^{-1} K^{-1} above 1000 K. Figure 10g–l shows the results of the nanostructured $In_{1.92}(ZnCe)_{0.08}O_3$ ceramics which were fabricated by co-precipitation and SPS [132]. A high *ZT* = 0.4 at 1050 K in the sample with a 50 nm grain size was achieved, ascribed to κ decreasing by 50% while maintaining a high σ. When the grain size is smaller than 20 nm, the *ZT* value is anticipated to approach 0.7.

To maximize $|S|$ and *PF*, it is preferable to utilize the energy-dependent scattering mechanism and scatter phonons more efficiently than electrons, as for a "PGEC" system. Therefore, the basic principle of this nanostructured method depends on the influence of the classical size effect and quantum effect on the electrons and phonons transport behavior. Although the classical size effects limit the mean free paths of phonons and electrons, quantum size effects (localization) may provide some beneficial changes in the transport properties of phonons and the electron states.
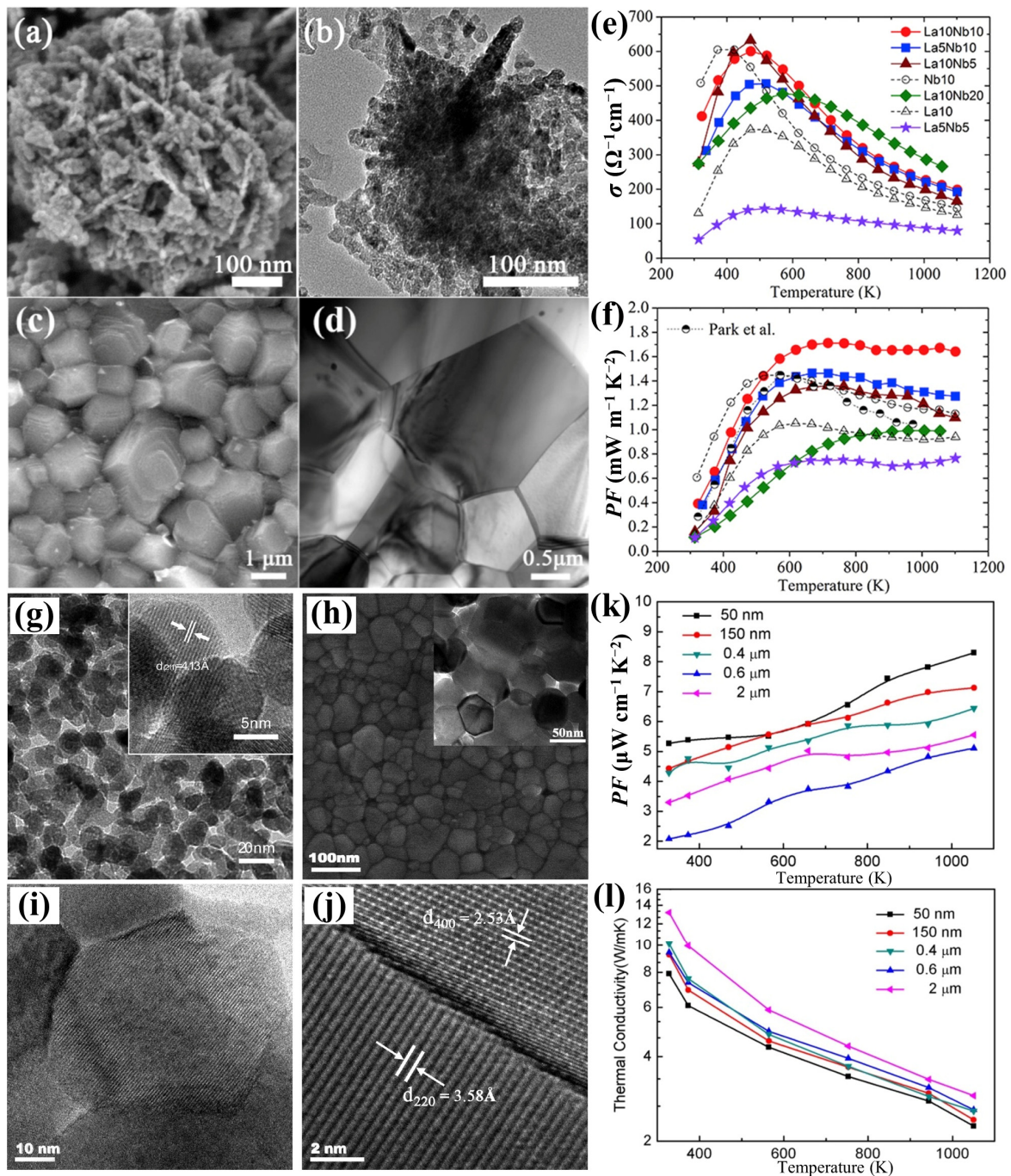
Figure 10. (**a**) SEM and (**b**) TEM image of powder; (**c**) SEM and (**d**) TEM image of bulk 10 mol% Nb-10 mol% La-doped $SrTiO_3$ bulk sample. Temperature dependence of (**e**) electrical conductivity and (**f**) power factor [36]. (**g**) The TEM image of $In_{1.92}(ZnCe)_{0.08}O_3$ nanopowder, (**h**) the SEM image of 50 nm grained sample. (**i**) TEM image at medium-magnification, (**j**) HRTEM image of the 50 nm grained sample. Temperature dependence of (**k**) power factor and (**l**) thermal conductivity for $In_{1.92}(ZnCe)_{0.08}O_3$ bulks with different grain sizes [132].

4.6. Textured Engineering

Texture engineering offers a strategy for gaining better thermoelectric performance in bulk ceramics by creating crystallographic anisotropy. Especially in layered crystal structure TEs, the electron and phonon transport properties are highly anisotropic. Multi-scale parallel interfaces, including zigzag interfaces and "core-shell" interfaces inside the orientation of the stripe-like grains, the paralleled grain boundaries, and lattice stacking

faults were observed in the "brick-wall" microstructure can contribute to suppressing the thermal conductivity [12,156]. The physical properties of this special crystallographic orientation in textured ceramics can approach 60–80% of the properties of single crystals of the same composition. Creating the textured structure helps to the decoupling of electrical and thermal properties. As an example shown in Figure 11a–k, $(Ca_{0.87}Ag_{0.1}La_{0.03})_3Co_4O_9$ textured ceramics with texture fraction of 0.93 [12] by template grain growth (TGG) method, the carrier concentration in the direction parallel to the tape casting is three times that of in the direction perpendicular to the tape casting, and the *PF* was achieved 0.64 mW/(m K^2) at 800 °C, which is 10 times that of in the direction perpendicular to the tape casting. The resultant κ_l = 0.37 W/(m·K) at 800 °C was obtained, which is 40% lower than that value parallel to the tape casting direction. As a result, the maximum *ZT* reached 0.43 at 800 °C, which was 1.2–3 times the *ZT* values in the vertical direction.
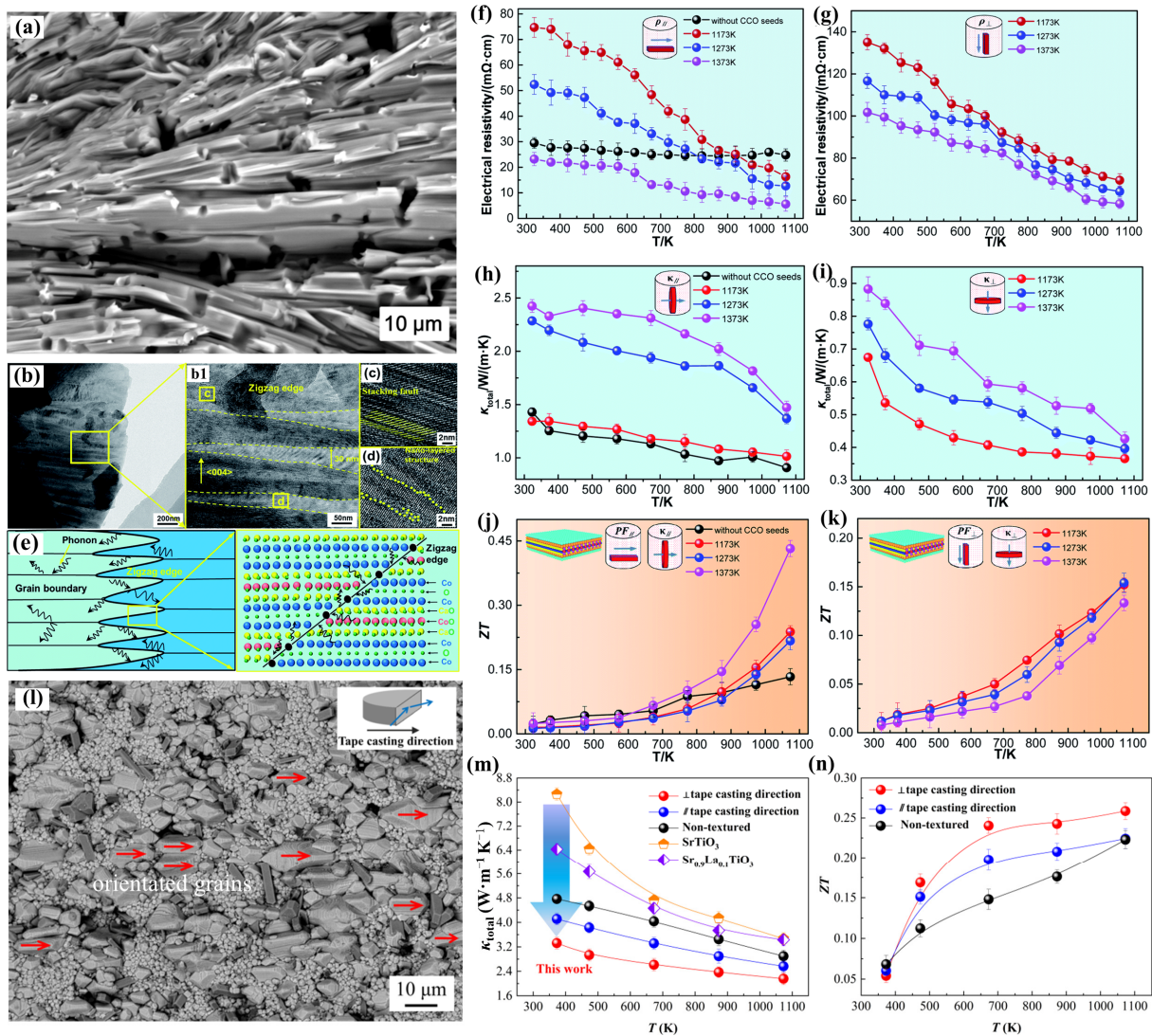

Figure 11. (**a**) BSE image, (**b**–**d**) TEM images, and (**e**) the sketch diagram of phonon scattering at the grain boundary and zigzag edge of the $(Ca_{0.87}Ag_{0.1}La_{0.03})_3Co_4O_9$ textured ceramics, and temperature dependence of the thermoelectric properties of the samples in parallel and perpendicular to the tape-casting direction. (**f**,**g**) Electrical resistivity, (**h**,**i**) thermal conductivity, (**j**,**k**) *ZT* values [12]. (**l**) BSE image, (**m**) Total thermal conductivity, and (**n**) *ZT* values of the $Sr_{0.9}La_{0.1}TiO_3$-based textured ceramic [156].

Figure 11l–n presents the textured $Sr_{0.9}La_{0.1}TiO_3$-based ceramics [156] with a texture fraction of 0.81, in which 10 wt.% plate-like $Sr_3Ti_2O_7$ template seeds served as templates for guiding epitaxial growth of grains combined with matrix powders of $Sr_{0.9}La_{0.1}TiO_3/20$ wt.%Ti to obtain the multi-scale interfaces decoupled electron and phonon transport performance to optimize ZT values. In the direction perpendicular to the tape casting direction, the maximum $ZT = 0.26$ was obtained at 1073 K. Comparing with the $SrTiO_3$, $Sr_{0.9}La_{0.1}TiO_3$, and the same composition of non-textured ceramics fabricated by the same sintering process, the lowest $\kappa_l = 1.9$ W/(m K) was obtained at 1073 K in the textured $Sr_{0.9}La_{0.1}TiO_3$-based ceramic which decreased by 40%, 38%, and 34%, respectively.

In the $Bi_{0.96}Pb_{0.04}CuSeO$ system [157], the significantly increased density of the interfaces generated along the pressure direction during the sintering process can effectively reduce κ_1; hence, the $ZT = 0.85$ at 840 K was achieved. In the textured $KSr_2Nb_5O_{15}$ ceramics [51,158], the power factor was significantly enhanced depending on different testing directions, such that it was 283 $\mu W/mK^2$ in perpendicular and 390 $\mu W/mK^2$ in parallel to the c direction at 1120 K. In summary, the above results indicate that the textured TE ceramics should both possess a high texture fraction and a narrow grains distribution for obtaining anisotropic thermal conductivity and high electrical conductivity.

4.7. Composites

For the ionic compound of oxide ceramics, their resistivity after doping modification, nanostructuring, or entropy engineering is still relatively high. To further reduce the resistivity of oxide ceramics, some compounds with excellent electrical conductivity, such as metal particles, graphene, and its derivatives, are added to the matrix to improve the thermoelectric properties.

M.J. Qin et al. added Bi_2O_3, nanosized Ag (30–40 nm in size), micro-sized Ti, and nano-sized Ti particles into the $Sr_{0.9}La_{0.1}TiO_3$ or $Ca_3Co_4O_9$ matrix to optimize the electrical and thermal properties [23,25,66]. These results demonstrate that the metal Ag and Bi/BiO_x located at grain boundaries can act as a conductive path between the adjacent $Sr_{0.9}La_{0.1}TiO_3$ and/or TiO_2 grains to improve the carrier mobility and serve as the phonon scattering centers to suppress κ_l. In the $Sr_{0.9}La_{0.1}TiO_3+20\%$ Ag composite system shown in Figure 12a–d, the conductive network illustrated in Figure 12d significantly increased σ to ~101.4 S cm^{-1} and the $|S|$ slightly improved to ~241 $\mu V K^{-1}$ at 883 K [25] simultaneously. The $(Ca_{0.9}Ag_{0.1})_3Co_4O_9$/nano-sized Ag composites [159] were fabricated by a two-step processing method of SPS combined with a heat–treatment and achieved the maximum $PF = 0.43$ mW/(m·K^2), $S = 196.90$ $\mu V/K$, the corresponding $\kappa_l = 1.86$ W/(m·K), and $ZT = 0.24$ at 1223 K. In the polycrystalline $SmBaCuFeO_{5+\delta}$/Ag composite ceramics [160], the hole concentration and mobility can be increased through the conductive effect of the second phases of copper oxides and Ag; thus, the obtained ZT value is about 16 times that of the pure $SmBaCuFeO_{5+\delta}$ sample.

The $Ca_3Co_4O_9$ and $Na_2Ca_2Nb_4O_{13}$ composite ceramic (Figure 12e) [161] can be prepared by uniaxial pressing of the mixed compound powders followed by a conventional sintering process with promising synergistic thermoelectric properties of $ZT = 0.32$ at 1073 K.

In addition, it has been confirmed that the 2D graphene can be introduced into $SrTiO_3$-based ceramics for grain refinement and promoting more oxygen vacancy formation to enhance carrier mobility [162]. Therefore, $SrTiO_3$-based ceramics containing graphite or its derivatives achieve single-crystal-like electron mobility [162–165] because the delocalization of Anderson localized electrons aided by graphite leads to a manifold improvement in weighted mobility and further the enhanced electron transport properties.
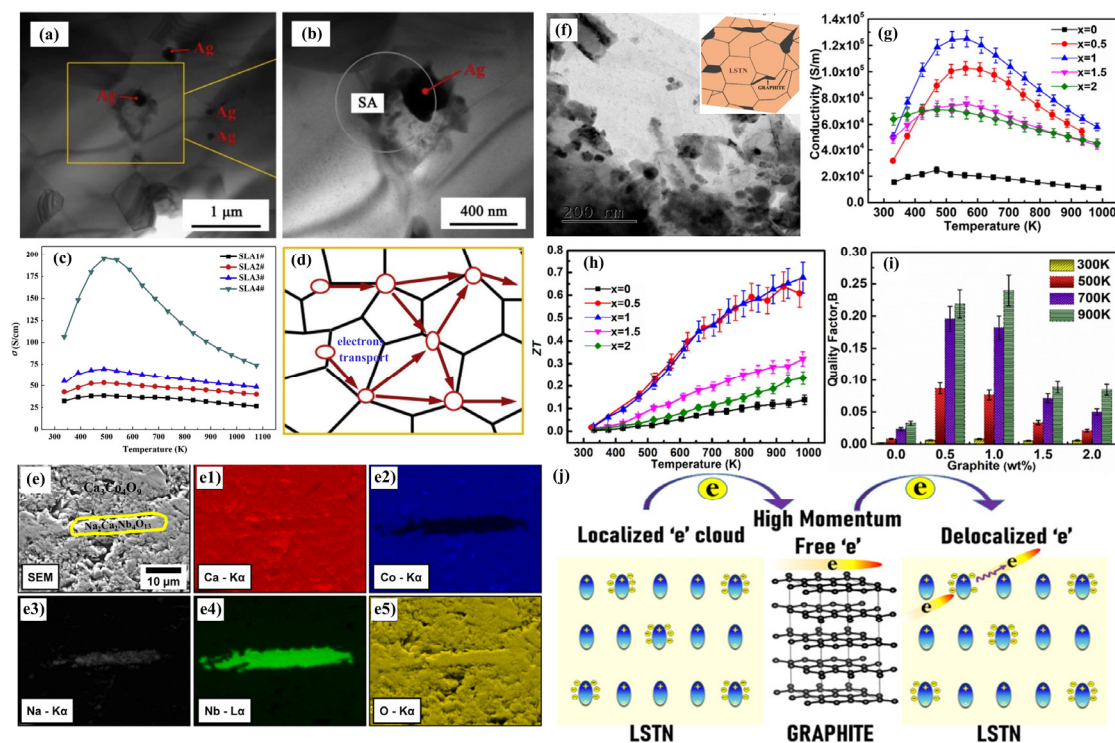
Figure 12. (**a**,**b**) TEM images, (**c**) temperature dependent on electrical conductivity, and (**d**) schematic diagram of the conductive network formed by Ag particles of $Sr_{0.9}La_{0.1}TiO_3/xAg$ samples [25]. (**e**) Cross-sectional SEM and (**e1**–**e5**) EDS elemental maps of the composite sample after sintering showing a single $Na_2Ca_2Nb_4O_{13}$ plate-like particle embedded in a $Ca_3Co_4O_9$ matrix [161]. (**f**) TEM image of dispersed $SrTi_{0.85}Nb_{0.15}O_3$ particles in graphite flakes (schematic of the $SrTi_{0.85}Nb_{0.15}O_3$ + graphite composite in the inset), (**g**) σ, (**h**) ZT values, (**i**) B factor, and (**j**) schematic of electrical transport promoted by G in the $SrTi_{0.85}Nb_{0.15}O_3$ + graphite composite sample [162].

In the matrix of $La_{0.07}Sr_{0.93}Ti_{0.93}Nb_{0.07}O_3$, graphite (G) was used to improve the electrical conductivity, and the maximum $ZT = 0.68$ is obtained (Figure 12f–j) [162]. In the nanostructured $SrTi_{0.85}Nb_{0.15}O_3$ composited with graphene oxide sample, the maximum $ZT = 0.5$ was attained at 1200K as a result of several orders increase of carrier mobility [165].

Ceramics of $Sr_{0.9}La_{0.1}TiO_3$ with additions of B_2O_3 [65] exhibit a core–shell-like structure resulting in a high $ZT = 0.39 \pm 0.03$. In $SrTiO_3$-TiO_2 biphase ceramics [166], a two-dimensional electron gas (2DEG) formed spontaneously on the heterointerface. Additionally, the addition of TiO_2 increases carrier mobility as well as carrier concentration by forming A-site cation vacancies. Therefore, a high $PF = 1.66\ mW/(m\ K^2)$ and $ZT = 0.24$ was achieved when the 25 wt% TiO_2 addition at 447 K.

In future research, one or more optimization strategies will be explored and expanded to improve the ZT values. Great efforts are required to pave the way for new oxide TEs exploration for the manufacture of the next generation of TE power generators for high-temperature applications.

5. Device Applications

Typically, a thermoelectric module consists of *p*-type and *n*-type TE legs and a metal electrode. Multiple thermoelectric modules need to be connected by wire to achieve the required output voltage, as shown in Figure 13 [167]. The thermoelectric device is usually made of a Cu electrode and alumina substrate, which is welded as the connection means to fix TE legs. The ceramic plates exhibit mechanical integrity and also act as electrical insulators for cooled and heated surfaces. Besides the commonly used Aluminum Oxide (Al_2O_3) ceramics, other ceramics, such as Beryllium Oxide (BeO) and Aluminum Nitride

(AlN), can also be employed. Electrode materials, besides the commonly used Cu and Ag, can also include Ni and alloy brazing materials, etc.
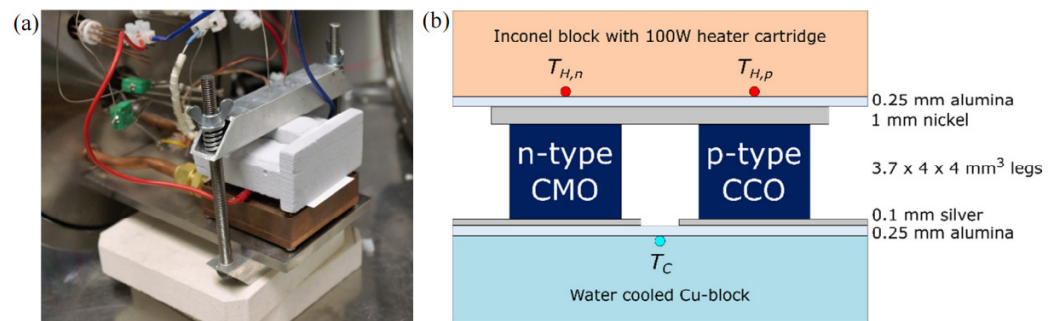

Figure 13. (**a**) Picture of the test device covering the connection and insulation board of the module above the water-cooled copper block. (**b**) Schematic diagram of module cross-section and test assembly with temperature measuring points [167].

Traditional thermoelectric device design has the following concerns. The first is to choose the appropriate *p*-type and *n*-type TEs which can be used in a wide temperature range, with high thermoelectric properties, high mechanical properties (Vickers hardness and fracture toughness), and high chemical stability. When the *p*-type and *n*-type TE legs of the thermoelectric module have different σ and κ, the two types of TE legs need to be designed with different geometric sizes [168]. In addition, it is necessary to pay attention to the connection between the TE legs and the electrode. An effective means is a reasonably well-designed sandwich. Electrode materials need to have high thermal conductivity and high electrical conductivity, and a similar expansion coefficient, with high bond strength, low contact resistance, and no serious diffusion reaction. To meet the above requirements, a multi-layer interface layer is usually introduced into the electrode, which can resist the element diffusion and chemical reaction, improve the connection strength, and minimize the interface resistance and thermal resistance [169].

5.1. Power Generation

In recent years, thermoelectric modules have attracted wide attention due to their great potential for power generation and electronic refrigeration. At present, oxide thermoelectric devices can be used in a wide temperature range, especially in high temperatures, but there are few types of research focused on oxide thermoelectric devices, and the efficiency and power of thermoelectric conversion still need to be further improved. Most of these modules are made of $Ca_3Co_4O_9$ as *p*-type materials, and the most common thermoelectric *n*-type oxides are $CaMnO_3$, $SrTiO_3$, ZnO, etc. [45]. TE modules usually adopt the silver bar and silver paste [170], Cu, Ni, etc., as electrode contacts.

Skomedal et al. [167] assembled *n*-type $CaMnO_3$ and *p*-type $Ca_3Co_4O_9$, which were sintered by discharge plasma into a thermoelectric module. The test setup is exhibited in Figure 13a, and the schematic diagram is shown in Figure 13b. It contains a water-cooled cooling block, an Inconel block with a 100 W heater, and two recesses for K-type thermocouples. Each module was slowly ramped up in steps of 200 °C up to a maximum hot side temperature of 800 °C. When the temperature difference is 760 °C, the maximum specific power output is 56 mW/cm^2, and the cycle test between 400 and 800 °C in a week shows that the power output is reduced by more than 50%, mainly because of cracks and oxidation layer formed near the nickel/oxide interface.

Choi et al. [171] use *n*-type $(ZnO)_7In_2O_3$ and layered *p*-type $Ca_3Co_4O_9$ legs to fabricate an oxid-based thermoelectric generator. The silver paste was printed on the top and bottom of each *p*-type $Ca_3Co_4O_9$ and *n*-type $(ZnO)_7In_2O_3$ leg by a screen printing method. At 1100 K, the *ZT* of thermoelectric properties of *p*-type and *n*-type legs are 0.55×10^{-4} and 1.35×10^{-4}, respectively. When a temperature difference is 673 K, the maximum power

obtained by 44 *p-n* modules is 423 mW. Funahashi et al. [172] tested the tensile and bending strength of a device consisting of *n*-type $CaMn_{0.98}Mo_{0.02}O_3$ and *p*-type $Ca_{2.7}Bi_{0.3}Co_4O_9$, silver paste, and two alumina substrates at room temperature. The *p*-type device reaches about 20 MPa when the pressure is 6.36 Mpa. The tensile strength of *n*-type devices is less than 10 Mpa. By measuring the thermoelectric generation properties of the module, including internal resistance, open circuit voltage, and output power, the performance of the module under thermal cycling and the vibration is tested. For the module under 6.36 Mpa, no deterioration of thermoelectric properties was observed within 10,000 h.

5.2. Sensor Devices

One of the primary applications of TEs is the temperature sensors, namely thermocouples, in which the temperature measurement of thin film thermocouples belongs to the contact in situ temperature measurement technology. For example, indium tin oxide (ITO) -In_2O_3 film thermocouple [173] have a limit measuring temperature reaching 1300 °C and the Seebeck coefficient reaches 160 μV/°C, the $MoSi_2$-Al_2O_3 and $TaSi_2$-Al_2O_3 thin film thermocouple [174] prepared by screen printing technology presented the thermoelectric output of 16 mV at the high-temperature stage. In addition, Saini et al. [175] used pulsed laser deposition technology to prepare on-chip thermoelectric film modules containing five pairs of *p*-type $Ca_3Co_4O_9$ and *n*-type $Al_{0.02}Zn_{0.98}O$ legs on alumina, $SrTiO_3$ single crystal, and fused silicon substrate and the maximum output power is 29.9 pW. The research and exploration of thermoelectric sensors are still in progress, and the oxide ceramic thin film thermoelectric modules are expected to be widely used in high-temperature thermoelectric sensors.

5.3. Flexibility and Wearable Devices

Flexible thermoelectric materials with excellent plastic deformation, light, inconspicuous, and other characteristics have a widespread application in portable electronic devices and wearable devices. Due to the ductility of inorganic semiconductors and ceramic insulators rarely observed, the application of inorganic oxides in flexible TEs field is rarely reported. Tian et al. [176] reported a flexible $Na_{1.4}Co_2O_4$ TE based on $Na_{1.4}Co_2O_4$ prepared and coated on printing paper by the self-flux method. The obtained thermoelectric material has S = 78–102 μV/K in the temperature range of 303–522 K. The PF = 159–223 $\mu Wm^{-1}K^{-2}$, which is superior to the Seebeck coefficient and power factor of other conducting polymers such as PEDOT and derivatives and their compounds.

5.4. Other Application

Other applications of thermoelectric modules include aerospace, automotive waste heat recovery systems, refrigeration, etc. At present, the application of alloy thermoelectric has been well-researched, while oxide needs to be further studied.

Recently, organic-inorganic composites and hybrid materials have promoted a flexible TE devices' design and exploration, which can be used in wearable electronic devices, and sensors to apply to the "Internet of Things" (IoT) field [177] with the spring-up and development of novel two-dimensional (2D) materials growth, superlattice growth, and inorganic-organic composites. Furthermore, using of high-performance nanostructured TEs combined with spectrally selective solar absorbers to develop solar thermoelectric generators (STEGs) obtained a peak efficiency of 4.6% [178], opening up the door to the comprehensive application of TEs for energy conversion.

6. Future Outlook

At present, the main problem faced by oxide TEs is still the relatively low thermoelectric conversion efficiency compared with alloy systems. For most oxides bulk TEs, the challenge focuses on poor electrical conductivity, especially low carrier mobility. The progress of relevant technologies and the strategies in other fields of alloy TEs provide many new optimizing directions and guidance for the oxide TEs, such as further exploring

the physical connotation of electricity and heat transport, predicting the corresponding results through theoretical calculation or/and machine learning, and analog simulation, which can also combine with experiments to prove each other to reduce the exploring time of new TE materials.

Rapidly developed strategies of high-entropy engineering, multi-scale interface engineering, defect chemistry, low-dimensionalization, nanoscale engineering, and quantum dot hybrid array thermoelectrics and/or their composite strategies emerged and expect to optimize thermoelectric performance. It is noteworthy that the 2D electronic gas (2DEG) system is an intriguing area of study that could expect to achieve a great breakthrough in thermoelectric performance. For example, at the interfaces between $SrTiO_3$ and other specific oxides such as TiO_2 or $LaAlO_3$, 2DEG can be created, and quantum confinements combined with the consequent energy filtering effects lead to the *ZT* beyond 2 [179].

The application of magnetic field, addition or combination of the quantum dot, and quantum effects in the low-dimensional semiconductors [180] can also be used to explore their effects in thermoelectric applications through reasonable regulation methods. In the near future, 3D printing technologies, direct ink writing, superstructures, and integration of structure and functionality will become important strategies in the TE fields for material research and development. The geometrical size and interfacial design of the modules and devices should be focused on for the develop high-efficiency devices in future work. In summary, oxide TEs with the advantages of chemical stability, oxidation resistance at high-temperature, and no toxic or volatile elements will have broad application prospects, such as industrial waste heat cycle, automobile exhaust gas utilization, etc.

Data Availability Statement: No new data were created or analyzed in this study. Data sharing is not applicable to this article.

Conflicts of Interest: The authors declare that they have no competing interests in this paper.

References

1. Zebarjadi, M.; Esfarjani, K.; Dresselhaus, M.S.; Ren, Z.F.; Chen, G. Perspectives on thermoelectrics: From fundamentals to device applications. *Energy Environ. Sci.* **2012**, *5*, 5147–5162. [CrossRef]
2. He, J.; Tritt, T.M. Advances in thermoelectric materials research: Looking back and moving forward. *Science* **2017**, *357*, eaak9997. [CrossRef] [PubMed]
3. Zhu, K.; Deng, B.; Zhang, P.X.; Kim, H.S.; Jiang, P.; Liu, W.S. System efficiency and power: The bridge between the device and system of a thermoelectric power generator. *Energy Environ. Sci.* **2020**, *13*, 3514–3526. [CrossRef]
4. Bu, Z.L.; Zhang, X.Y.; Hu, Y.X.; Chen, Z.W.; Lin, S.Q.; Li, W.; Xiao, C.; Pei, Y.Z. A record thermoelectric efficiency in tellurium-free modules for low-grade waste heat recovery. *Nat. Commun.* **2022**, *13*, 237. [CrossRef] [PubMed]
5. Biswas, K.; He, J.Q.; Blum, I.D.; Wu, C.; Hogan, T.P.; Seidman, D.N.; Dravid, V.P.; Kanatzidis, M.G. High-performance bulk thermoelectrics with all-scale hierarchical architectures. *Nature* **2012**, *489*, 414–418. [CrossRef] [PubMed]
6. Altenkirch, E. Elektrothermische Kälteerzeugung und reversible elektrische Heizung. *Phys. Z.* **1911**, *12*, 920–924.
7. Goupil, C.; Seifert, W.; Zabrocki, K.; Müller, E.; Snyder, G.J. Thermodynamics of thermoelectric phenomena and applications. *Entropy* **2011**, *13*, 1481–1517. [CrossRef]
8. Fergus, J.W. Oxide materials for high temperature thermoelectric energy conversion. *J. Eur. Ceram. Soc.* **2012**, *32*, 525–540. [CrossRef]

9. Ohta, H.; Sugiura, K.; Koumoto, K. Recent progress in oxide thermoelectric materials: P-type $Ca_3Co_4O_9$ and n-type $SrTiO_3$. *Inorg. Chem.* **2008**, *47*, 8429–8436. [CrossRef]

10. Bittner, M.; Helmich, L.; Nietschke, F.; Geppert, B.; Oeckler, O.; Feldhoff, A. Porous $Ca_3Co_4O_9$ with enhanced thermoelectric properties derived from sol-gel synthesis. *J. Eur. Ceram. Soc.* **2017**, *37*, 3909–3915. [CrossRef]

11. Xu, J.; Wei, C.P.; Jia, K. Thermoelectric performance of textured $Ca_{3-x}Yb_xCo_4O_{9-\delta}$ ceramics. *J. Alloys Compd.* **2010**, *500*, 227–230. [CrossRef]

12. Shi, Z.M.; Su, T.C.; Zhang, P.; Lou, Z.H.; Qin, M.J.; Gao, T.; Xu, J.; Zhu, J.H.; Gao, F. Enhanced thermoelectric performance of $Ca_3Co_4O_9$ ceramics through grain orientation and interface modulation. *J. Mater. Chem. A* **2020**, *8*, 19561–19572. [CrossRef]

13. Nong, N.V.; Liu, C.J.; Ohtaki, M. Improvement on the high temperature thermoelectric performance of Ga-doped misfit-layered $Ca_3Co_{4-x}Ga_xO_{9+\delta}$ (x = 0, 0.05, 0.1, and 0.2). *J. Alloys Compd.* **2010**, *491*, 53–56. [CrossRef]

14. Shi, Z.M.; Wang, L.X.; Li, L.L.; Wei, J.; Tong, S.J.; Zhang, J.Z.; Li, X.T.; Guo, Y.P.; Zhang, Y. Joint effect of Bi_2O_3 and CuO additives in regulating the thermoelectric properties of $(Ca_{0.87}Ag_{0.1}Dy_{0.03})_3Co_4O_9$ composite ceramics. *Mater. Sci. Eng. B* **2023**, *290*, 116311. [CrossRef]

15. Shi, Z.M.; Xu, J.; Zhu, J.H.; Zhang, Y.; Gao, T.; Qin, M.J.; Sun, H.; Dong, G.G.; Gao, F. Effect of platelet template seeds on microstructure and thermoelectric properties of $Ca_3Co_4O_9$ ceramics. *Ceram. Int.* **2019**, *45*, 1977–1983. [CrossRef]

16. Assadi, M.H.N.; Katayama-Yoshida, H. Restoration of long range order of Na ions in Na_xCoO_2 at high temperatures by sodium site doping. *Comput. Mater. Sci.* **2015**, *109*, 308–311. [CrossRef]

17. Wang, Y.L.; Ni, J. Ground state structure of sodium ions in Na_xCoO_2: A combined Monte Carlo and first-principles approach. *Phys. Rev. B* **2007**, *76*, 094101. [CrossRef]

18. Koumoto, K.; Terasaki, I.; Funahashi, R. Complex oxide materials for potential thermoelectric applications. *MRS Bull.* **2006**, *31*, 206–210. [CrossRef]

19. Roger, M.; Morris, D.J.P.; Tennant, D.A.; Gutmann, M.J.; Goff, J.P.; Hoffmann, J.U.; Feyerherm, R.; Dudzik, E.; Prabhakaran, D.; Boothroyd, A.T.; et al. Patterning of sodium ions and the control of electrons in sodium cobaltate. *Nature* **2007**, *445*, 631–634. [CrossRef]

20. Zhao, L.D.; He, J.Q.; Berardan, D.; Lin, Y.H.; Li, J.F.; Nan, C.W.; Drago, N. BiCuSeO oxyselenides: New promising thermoelectric materials. *Energy Environ. Sci.* **2014**, *7*, 2900–2924. [CrossRef]

21. Liu, Y.; Zhao, L.D.; Zhu, Y.C.; Liu, Y.C.; Li, F.; Yu, M.J.; Liu, D.B.; Xu, W.; Lin, Y.H.; Nan, C.W. Synergistically optimizing electrical and thermal transport properties of BiCuSeO via a dual-doping approach. *Adv. Energy Mater.* **2016**, *6*, 1502423. [CrossRef]

22. Yang, D.W.; Su, X.L.; Yan, Y.G.; Hu, T.Z.; Xie, H.Y.; He, J.; Uher, C.; Kanatzidis, M.G.; Tang, X.F. Manipulating the combustion wave during self-propagating synthesis for high thermoelectric performance of layered oxychalcogenide $Bi_{1-x}Pb_xCuSeO$. *Chem. Mater.* **2016**, *28*, 4628–4640. [CrossRef]

23. Qin, M.J.; Lou, Z.H.; Zhang, P.; Shi, Z.M.; Xu, J.; Chen, Y.S.; Gao, F. Enhancement of thermoelectric performance of $Sr_{0.9}La_{0.1}TiO_3$-based ceramics regulated by nanostructures. *ACS Appl. Mater. Interfaces* **2020**, *48*, 53899–53909. [CrossRef] [PubMed]

24. Zhang, B.Y.; Wang, J.; Zou, T.; Zhang, S.; Yaer, X.B.; Ding, N.; Liu, C.Y.; Miao, L.; Li, Y.; Wu, Y. High thermoelectric performance of Nb-doped $SrTiO_3$ bulk materials with different doping levels. *J. Mater. Chem. C* **2015**, *3*, 11406–11411. [CrossRef]

25. Qin, M.J.; Gao, F.; Dong, G.G.; Xu, J.; Fu, M.S.; Wang, Y.; Reece, M.; Yan, H.X. Microstructure characterization and thermoelectric properties of $Sr_{0.9}La_{0.1}TiO_3$ ceramics with nano-sized Ag as additive. *J. Alloys Compd.* **2018**, *762*, 80–89. [CrossRef]

26. Devi, N.Y.; Vijayakumar, K.; Rajasekaran, P.; Nedunchezhian, A.S.A.; Sidharth, D.; Masaru, S.; Arivanandhan, M.; Jayavel, R. Effect of Gd and Nb co-substitution on enhancing the thermoelectric power factor of nanostructured $SrTiO_3$. *Ceram. Int.* **2021**, *47*, 3201–3208. [CrossRef]

27. Fu, Q.Q.; Gu, H.; Xing, J.J.; Cao, Z.; Wang, J. Controlling the A-site deficiency and oxygen vacancies by donor-doping in pre-reductive-sintered thermoelectric $SrTiO_3$ ceramics. *Acta. Mater.* **2022**, *229*, 117785. [CrossRef]

28. Zhan, B.; Lan, J.L.; Liu, Y.C.; Lin, Y.H.; Shen, Y.; Nan, C.W. High temperature thermoelectric properties of Dy-doped $CaMnO_3$ ceramics. *J. Mater. Sci. Technol.* **2014**, *30*, 821–825. [CrossRef]

29. Zhang, F.P.; Lu, Q.M.; Zhang, X.; Zhang, J.X. First principle investigation of electronic structure of $CaMnO_3$ thermoelectric compound oxide. *J. Alloys Compd.* **2011**, *509*, 542–545. [CrossRef]

30. Li, J.B.; Wang, Y.X.; Yang, X.; Kang, H.J.; Cao, Z.Q.; Jiang, X.; Chen, Z.N.; Guo, E.Y.; Wang, T.M. Processing bulk insulating $CaTiO_3$ into a high-performance thermoelectric material. *Chem. Eng. J.* **2022**, *428*, 131121. [CrossRef]

31. Zhang, R.Z.; Hu, X.Y.; Guo, P.; Wang, C.L. Thermoelectric transport coefficients of n-doped $CaTiO_3$, $SrTiO_3$ and $BaTiO_3$: A theoretical study. *Phys. B Condens. Matter* **2012**, *407*, 1114–1118. [CrossRef]

32. Zhu, B.B.; Zhang, T.S.; Tian, R.M.; Tan, T.T.; Donelson, R.; Li, S. Enhancement of thermoelectric properties in Sn doped $(In_{0.95}Lu_{0.05})_2O_3$. *J. Alloys Compd.* **2015**, *644*, 119–123. [CrossRef]

33. Lan, J.L.; Liu, Y.C.; Lin, Y.H.; Nan, C.W.; Cai, Q.; Yang, X.P. Enhanced thermoelectric performance of In_2O_3-based ceramics via nanostructuring and point defect engineering. *Sci. Rep.* **2015**, *5*, 7783. [CrossRef]

34. Zhu, B.B.; Chen, C.; Yao, Z.C.; Chen, J.Y.; Jia, C.; Wang, Z.H.; Tian, R.M.; Tao, L.; Xue, F.; Hng, H.H. Multiple doped ZnO with enhanced thermoelectric properties. *J. Eur. Ceram. Soc.* **2021**, *41*, 4182–4188. [CrossRef]

35. Arias-Serrano, B.I.; Mikhalev, S.M.; Ferro, M.C.; Tobaldi, D.M.; Frade, J.R.; Kovalevsky, A.V. On the high-temperature degradation mechanism of ZnO-based thermoelectrics. *J. Eur. Ceram. Soc.* **2021**, *41*, 1730–1734. [CrossRef]

36. Wang, J.; Zhang, B.Y.; Kang, H.J.; Li, Y.; Yaer, X.B.; Li, J.F.; Tan, Q.; Zhang, S.; Fan, G.H.; Liu, C.Y.; et al. Record high thermoelectric performance in bulk SrTiO$_3$ via nano-scale modulation doping. *Nano Energy* **2017**, *35*, 387–395. [CrossRef]

37. Kim, H.S.; Gibbs, Z.M.; Tang, Y.L.; Wang, H.; Snyder, G.J. Characterization of Lorenz number with Seebeck coefficient measurement. *APL Mater.* **2015**, *3*, 041506. [CrossRef]

38. Qin, Y.X.; Xiao, Y.; Zhao, L.D. Carrier mobility does matter for enhancing thermoelectric performance. *APL Mater.* **2020**, *8*, 010901. [CrossRef]

39. Takabatake, T.; Suekuni, K.; Nakayama, T.; Kaneshita, E. Phonon-glass electron-crystal thermoelectric clathrates: Experiments and theory. *Rev. Mod. Phys.* **2014**, *86*, 669–716. [CrossRef]

40. Mitchell, R.H.; Chakhmouradian, A.R.; Woodward, P.M. Crystal chemistry of perovskite-type compounds in the tausonite-loparite series, (Sr$_{1-2x}$Na$_x$La$_x$)TiO$_3$. *Phys. Chem. Miner.* **2000**, *27*, 583–589. [CrossRef]

41. Nelmes, R.J.; Meyer, G.M.; Hutton, J. Thermal motion in SrTiO$_3$ at room temperature: Anharmonic or disordered? *Ferroelectrics* **1978**, *21*, 461–462. [CrossRef]

42. Samanta, P.K.; Chaudhuri, P.R. Substrate effect on morphology and photoluminescence from ZnO monopods and bipods. *Front. Optoelectron.* **2011**, *4*, 130–136. [CrossRef]

43. Schröer, P.; Krüger, P.; Pollmann, J. First-principles calculation of the electronic structure of the wurtzite semiconductors ZnO and ZnS. *Phys. Rev. B* **1993**, *47*, 6971–6980. [CrossRef]

44. Florescu, D.I.; Mourokh, L.G.; Pollak, F.H.; Look, D.C.; Cantwell, G.; Li, X. High spatial resolution thermal conductivity of bulk ZnO (0001). *J. Appl. Phys.* **2002**, *91*, 890–892. [CrossRef]

45. Yin, Y.N.; Tudu, B.; Tiwari, A. Recent advances in oxide thermoelectric materials and modules. *Vacuum* **2017**, *146*, 356–374. [CrossRef]

46. Imada, M.; Fujimori, A.; Tokura, Y. Metal-insulator transitions. *Rev. Mod. Phys.* **1998**, *70*, 1039–1263. [CrossRef]

47. Loshkareva, N.N.; Nomerovannaya, L.V.; Mostovshchikova, E.V.; Makhnev, A.A.; Sukhorukov, Y.P.; Solin, N.I.; Arbuzova, T.I.; Naumov, S.V.; Kostromitina, N.V.; Balbashov, A.M.; et al. Electronic structure and polarons in CaMnO$_{3-\delta}$ single crystals: Optical data. *Phys. Rev. B* **2004**, *70*, 224406. [CrossRef]

48. Yang, W.C.; Zhang, H.C.; Tao, P.G.; Zhang, D.D.; Zhang, D.W.; Wang, Z.H.; Tang, G.D. Optimization of the spin entropy by incorporating magnetic ion in a misfit-layered calcium cobaltite. *Ceram. Int.* **2016**, *42*, 9744–9748. [CrossRef]

49. Wu, T.; Tyson, T.A.; Bai, J.M.; Pandya, K.; Jaye, C.; Fischer, D. On the origin of enhanced thermoelectricity in Fe doped Ca$_3$Co$_4$O$_9$. *J. Mater. Chem. C* **2013**, *1*, 4114–4121. [CrossRef]

50. Koshibae, W.; Maekawa, S. Effects of spin and orbital degeneracy on the thermopower of strongly correlated systems. *Phys. Rev. Lett.* **2001**, *87*, 236603. [CrossRef]

51. Duran, C.; Yildiz, A.; Dursun, S.; Mackey, J.; Sehirlioglu, A. Thermoelectric characteristics of textured KSr$_2$Nb$_5$O$_{15}$ ceramics. *Scr. Mater.* **2016**, *112*, 114–117. [CrossRef]

52. Liu, H.Q.; Ma, H.A.; Su, T.C.; Zhang, Y.W.; Sun, B.; Liu, B.W.; Kong, L.J.; Liu, B.M.; Jia, X.P. High-thermoelectric performance of TiO$_{2-x}$ fabricated under high pressure at high temperatures. *J. Mater.* **2017**, *3*, 286–292.

53. Fujita, K.; Mochida, T.; Nakamura, K. High-temperature thermoelectric properties of Na$_x$CoO$_2$-delta single crystals. *Jpn. J. Appl. Phys.* **2001**, *40*, 4644–4647. [CrossRef]

54. Shikano, M.; Funahashi, R. Electrical and thermal properties of single-crystalline (Ca$_2$CoO$_3$)$_{0.7}$CoO$_2$ with a Ca$_3$Co$_4$O$_9$ structure. *Appl. Phys. Lett.* **2003**, *82*, 1851–1853. [CrossRef]

55. Kovalevsky, A.V.; Aguirre, M.H.; Populoh, S.; Patricio, S.G.; Ferreira, N.M.; Mikhalev, S.M.; Fagg, D.P.; Weidenkaff, A.; Frade, J.R. Designing strontium titanate-based thermoelectrics: Insight into defect chemistry mechanisms. *J. Mater. Chem. A* **2017**, *5*, 3909–3922. [CrossRef]

56. Hassanin, H.; Jiang, K. Net shape manufacturing of ceramic micro parts with tailored graded layers. *J. Micromech. Microeng.* **2014**, *24*, 015018. [CrossRef]

57. Hassanina, H.; Jiang, K. Fabrication and characterization of stabilised zirconia micro parts via slip casting and soft moulding. *Scr. Mater.* **2013**, *69*, 433–436. [CrossRef]

58. Wang, T.; Nan, P.F.; Wang, H.C.; Wang, H.; Su, W.; Sotelo, A.; Zhai, J.Z.; Wang, X.; Ran, Y.Z.; Chen, T.T.; et al. Right heterogeneous microstructure for achieving excellent thermoelectric performance in Ca$_{0.9}$R$_{0.1}$MnO$_{3-\delta}$(R.=Dy, Yb) Ceramics. *Inorg. Chem.* **2018**, *57*, 9133–9141. [CrossRef]

59. Zhang, P.; Lou, Z.H.; Qin, M.H.; Xu, J.; Zhu, J.T.; Shi, Z.M.; Chen, Q.; Reece, M.J.; Yan, H.X.; Gao, F. High-entropy (Ca$_{0.2}$Sr$_{0.2}$Ba$_{0.2}$La$_{0.2}$Pb$_{0.2}$)TiO$_3$ perovskite ceramics with A-site short-range disorder for thermoelectric applications. *J. Mater. Sci. Technol.* **2022**, *97*, 182–189. [CrossRef]

60. Kovalevsky, A.V.; Yaremchenko, A.A.; Populoh, S.; Populoh, S.; Frade, J.R. Enhancement of thermoelectric performance in strontium titanate by praseodymium substitution. *J. Appl. Phys.* **2013**, *113*, 053704. [CrossRef]

61. Lou, Z.H.; Zhang, P.; Gong, L.Y.; Xu, J.; Gong, L.Y.; Reece, M.J.; Yan, H.X.; Gao, F. A novel high-entropy perovskite ceramics Sr$_{0.9}$La$_{0.1}$(Zr$_{0.25}$Sn$_{0.25}$Ti$_{0.25}$Hf$_{0.25}$)O$_3$ with low thermal conductivity and high Seebeck coefficient. *J. Eur. Ceram. Soc.* **2022**, *42*, 3480–3488. [CrossRef]

62. Han, J.; Song, Y.; Liu, X.; Wang, F.P. Sintering behavior and thermoelectric properties of LaCoO$_3$ ceramics with Bi$_2$O$_3$-B$_2$O$_3$-SiO$_2$ as a sintering aid. *RSC Adv.* **2014**, *4*, 51995–52000. [CrossRef]

63. Alvarez-Ruiz, D.T.; Azough, F.; Hernandez-Maldonado, D.; Kepaptsoglou, D.M.; Ramasse, Q.M.; Day, S.J.; Svec, P.; Svec, P.; Freer, R. Utilising unit-cell twinning operators to reduce lattice thermal conductivity in modular structures: Structure and thermoelectric properties of $Ga_2O_3(ZnO)_9$. *J. Alloys Compd.* **2018**, *762*, 892–900. [CrossRef]

64. Nishiyama, S.; Ichikawa, A.; Hattori, T. Thermoelectric properties of CuO-added $AgSbO_3$ ceramics. *J. Ceram. Soc. Jpn.* **2004**, *112*, 298–300. [CrossRef]

65. Azough, F.; Gholinia, A.; Alvarez-Ruiz, D.T.; Duran, E.; Kepaptsoglou, D.M.; Eggeman, A.S.; Ramasse, Q.M.; Freer, R. Self-nanostructuring in $SrTiO_3$: A novel strategy for enhancement of thermoelectric response in oxides. *ACS Appl. Mater. Interfaces* **2019**, *11*, 32833–32843. [CrossRef]

66. Shi, Z.M.; Gao, F.; Zhu, J.H.; Xu, J.; Zhang, Y.; Gao, T.; Qin, M.J. Influence of liquid-phase sintering on microstructure and thermoelectric properties of $Ca_3Co_4O_9$-based ceramics with Bi_2O_3 additive. *J. Mater.* **2019**, *5*, 711–720. [CrossRef]

67. Wang, Y.F.; Zhang, X.Y.; Shen, L.M.; Bao, N.Z.; Wan, C.L.; Park, N.H.; Koumoto, K.; Gupta, A. Nb-doped grain boundary induced thermoelectric power factor enhancement in La-doped $SrTiO_3$ nanoceramics. *J. Power Sources* **2013**, *241*, 255–258. [CrossRef]

68. Tian, T.; Cheng, L.H.; Xing, J.J.; Zheng, L.Y.; Man, Z.Y.; Hu, D.L.; Bernik, S.; Zeng, J.T.; Yang, J.; Liu, Y. Effects of sintering on the microstructure and electrical properties of ZnO-based thermoelectric materials. *Mater. Des.* **2017**, *132*, 479–485. [CrossRef]

69. Diaz-Chao, P.; Giovannelli, F.; Lebedev, O.; Chateigner, D.; Lutterotti, L.; Delorme, F.; Guilmeau, E. Textured Al-doped ZnO ceramics with isotropic grains. *J. Eur. Ceram. Soc.* **2014**, *34*, 4247–4256. [CrossRef]

70. Qin, M.J.; Lou, Z.J.; Shi, Z.J.; Zhang, R.J.; Xu, J.; Gao, F. Enhanced thermoelectric properties of $Sr_{0.9}La_{0.1}TiO_3$ ceramics fabricated by SPS with nanosized Ti addition. *J. Mater. Sci.-Mater. Electron.* **2020**, *31*, 6919–6926. [CrossRef]

71. Chen, Y.X.; Shi, K.D.; Li, F.; Xu, X.; Ge, Z.H.; He, J.Q. Highly enhanced thermoelectric performance in BiCuSeO ceramics realized by Pb doping and introducing Cu deficiencies. *J. Am. Ceram. Soc.* **2019**, *102*, 5989–5996. [CrossRef]

72. Jeong, A.; Suekuni, K.; Ohtaki, M.; Jang, B.K. Thermoelectric properties of In- and Ga-doped spark plasma sintered ZnO ceramics. *Ceram. Int.* **2021**, *47*, 23927–23934. [CrossRef]

73. Mori, T. Novel principles and nanostructuring methods for enhanced thermoelectrics. *Small* **2017**, *13*, 1702013. [CrossRef]

74. Ito, M.; Ohira, N. Effects of TiB_2 addition on spark plasma sintering and thermoelectric performance of Y-doped $SrTiO_3$ synthesized by polymerized complex process. *Compos. Part B Eng.* **2016**, *88*, 108–113. [CrossRef]

75. Novitskii, A.; Guelou, G.; Voronin, A.; Mori, T.; Khovaylo, V. Direct synthesis of p-type bulk BiCuSeO oxyselenides by reactive spark plasma sintering and related thermoelectric properties. *Scr. Mater.* **2020**, *187*, 317–322. [CrossRef]

76. Liu, D.Q.; Zhang, Y.W.; Kang, H.J.; Li, J.L.; Chen, Z.N.; Wang, T.M. Direct preparation of La-doped $SrTiO_3$ thermoelectric materials by mechanical alloying with carbon burial sintering. *J. Eur. Ceram. Soc.* **2018**, *38*, 807–811. [CrossRef]

77. Feng, B.; Li, G.Q.; Pan, Z.; Hu, X.M.; Liu, P.H.; He, Z.; Li, Y.W.; Fan, X.A. Effect of synthesis processes on the thermoelectric properties of BiCuSeO oxyselenides. *J. Alloys Compd.* **2018**, *754*, 131–138. [CrossRef]

78. Park, K.; Son, J.S.; Woo, S.I.; Shin, K.; Oh, M.W.; Park, S.D.; Hyeon, T. Colloidal synthesis and thermoelectric properties of La-doped $SrTiO_3$ nanoparticles. *J. Mater. Chem. A* **2014**, *2*, 4217–4224. [CrossRef]

79. Yue, Z.W.; Ji, X.L.; Zhou, W.; Ji, Z.H.; Guo, F. Enhanced thermoelectric performance of hydrothermal synthesized Ag incorporated $Cu_{2-x}S$ micro/nano composites. *Ceram. Int.* **2023**, *49*, 8428–8434. [CrossRef]

80. Baghbanzadeh, M.; Carbone, L.; Cozzoli, P.D.; Kappe, C.O. Microwave-assisted synthesis of colloidal inorganic nanocrystals. *Angew. Chem. Int. Ed.* **2011**, *50*, 11312–11359. [CrossRef]

81. Park, D.; Ju, H.; Kim, J. One-pot fabrication of Ag-$SrTiO_3$ nanocomposite and its enhanced thermoelectric properties. *Ceram. Int.* **2019**, *45*, 16969–16975. [CrossRef]

82. Mehta, R.J.; Zhang, Y.L.; Karthik, C.; Singh, B.; Siegel, R.W.; Borca-Tasciuc, T.; Ramanath, G. A new class of doped nanobulk high-figure-of-merit thermoelectrics by scalable bottom-up assembly. *Nat. Mater.* **2012**, *11*, 233–240. [CrossRef] [PubMed]

83. Populoh, S.; Trottmann, M.; Aguire, M.H.; Weidenkaff, A. Nanostructured Nb-substituted $CaMnO_3$ n-type thermoelectric material prepared in a continuous process by ultrasonic spray combustion. *J. Mater. Res.* **2011**, *26*, 1947–1952. [CrossRef]

84. Sun, Y.F.; Cheng, H.; Gao, S.; Liu, Q.H.; Sun, Z.H.; Xiao, C.; Wu, C.Z.; Wei, S.P.; Xie, Y. Atomically thick bismuth selenide freestanding single layers achieving enhanced thermoelectric energy harvesting. *J. Am. Chem. Soc.* **2012**, *134*, 20294–20297. [CrossRef] [PubMed]

85. Samanta, M.; Guin, S.N.; Biswas, K. Ultrathin few layer oxychalcogenide BiCuSeO nanosheets. *Inorg. Chem. Front.* **2017**, *4*, 84–90. [CrossRef]

86. Dehkordi, A.M.; Zebarjadi, M.; He, J.; Tritt, T.M. Thermoelectric power factor: Enhancement mechanisms and strategies for higher performance thermoelectric materials. *Mater. Sci. Eng. R* **2015**, *97*, 1–22. [CrossRef]

87. Ren, G.K.; Lan, J.L.; Zhao, L.D.; Liu, C.; Yuan, H.C.; Shi, Y.; Zhou, Z.F.; Lin, Y.H. Layered oxygen-containing thermoelectric materials: Mechanisms, strategies, and beyond. *Mater. Today* **2019**, *29*, 68–85. [CrossRef]

88. Chen, Q.; Zhang, P.; Qin, M.J.; Lou, Z.H.; Gong, L.Y.; Xu, J.; Kong, J.; Yan, H.X.; Gao, F. Effect of La^{3+}, Ag^+ and Bi^{3+} doping on thermoelectric properties of $SrTiO_3$: First-principles investigation. *Ceram. Int.* **2022**, *48*, 13803–13816. [CrossRef]

89. Benthem, K.V.; Elsässer, C.; French, R.H. Bulk electronic structure of $SrTiO_3$: Experiment and theory. *J. Appl. Phys.* **2001**, *90*, 6156–6164. [CrossRef]

90. Fumega, A.O.; Fu, Y.H.; Pardo, V.; Singh, D.J. Understanding the lattice thermal conductivity of $SrTiO_3$ from an ab initio perspective. *Phys. Rev. Mater.* **2020**, *4*, 033606. [CrossRef]

91. Kovalevsky, A.V.; Yaremchenko, A.A.; Populoh, S.; Thiel, P.; Fagg, D.P.; Weidenkaff, A.; Frade, J.R. Towards a high thermoelectric performance in rare-earth substituted SrTiO₃: Effects provided by strongly-reducing sintering conditions. *Phys. Chem. Chem. Phys.* **2014**, *16*, 26946–26954. [CrossRef] [PubMed]

92. Putri, Y.E.; Said, S.M.; Refinel, R.; Ohtaki, M.; Syukri, S. Low thermal conductivity of RE-doped SrO(SrTiO₃)₁ Ruddlesden Popper phase bulk materials prepared by molten salt method. *Electron. Mater. Lett.* **2018**, *14*, 556–562. [CrossRef]

93. Kahalya, M.U.; Schwingenschlögl, U. Thermoelectric performance enhancement of SrTiO₃ by Pr doping. *J. Mater. Chem. A* **2014**, *2*, 10379–10383. [CrossRef]

94. Cui, Y.; Salvador, J.R.; Yang, J.; Wang, H.; Amow, G.; Kleinke, H. Thermoelectric properties of heavily doped n-type SrTiO₃ bulk materials. *J. Electron. Mater.* **2009**, *38*, 1002–1007. [CrossRef]

95. Kovalevsky, A.V.; Populoh, S.; Patrício, S.G.; Thiel, P.; Ferro, M.C.; Fagg, D.P.; Frade, J.R.; Weidenkaff, A. Design of SrTiO₃-based thermoelectrics by tungsten substitution. *J. Phys. Chem. C* **2015**, *119*, 4466–4478. [CrossRef]

96. Singsoog, K.; Seetawan, T.; Vora-Ud, A.; Thanachayanont, C. Theoretical enhancement of thermoelectric properties of Sr₁₋ₓLaₓTiO₃. *Integr. Ferroelectr.* **2014**, *155*, 111–118. [CrossRef]

97. Liu, J.; Wang, C.L.; Li, Y.; Su, W.B.; Zhu, Y.H.; Li, J.C.; Mei, L.M. Influence of rare earth doping on thermoelectric properties of SrTiO₃ ceramics. *J. Appl. Phys.* **2013**, *114*, 223714. [CrossRef]

98. Lin, J.H.; Hwang, C.S.; Sie, F.R. Preparation and thermoelectric properties of Nd and Dy co-doped SrTiO₃ bulk materials. *Mater. Res. Bull.* **2020**, *122*, 110650. [CrossRef]

99. Flahaut, D.; Mihara, T.; Funahashi, R.; Nabeshima, N.; Lee, K.; Ohta, H.; Koumoto, K. Thermoelectrical properties of *A*-site substituted Ca₁₋ₓReₓMnO₃ system. *J. Appl. Phys.* **2006**, *100*, 084911. [CrossRef]

100. Sanmathi, C.S.; Takahashi, Y.; Sawaki, D.; Klein, Y.; Retoux, R.; Terasaki, I.; Noudem, J.G. Microstructure control on thermoelectric properties of Ca₀.₉₆Sm₀.₀₄MnO₃ synthesised by co-precipitation technique. *Mater. Res. Bull.* **2010**, *45*, 558. [CrossRef]

101. Kabir, R.; Tian, R.M.; Zhang, T.S.; Donelson, R.; Tan, T.T.; Li, S. Role of Bi doping in thermoelectric properties of CaMnO₃. *J. Alloys Compd.* **2015**, *628*, 347–351. [CrossRef]

102. Kuganathan, N.; Chroneos, A. Defect and dopant properties in CaMnO₃. *AIP Adv.* **2021**, *11*, 055106. [CrossRef]

103. Xu, G.J.; Funahashi, R.; Pu, Q.R.; Liu, B.; Tao, R.H.; Wang, G.S.; Ding, Z.J. High-temperature transport properties of Nb and Ta substituted CaMnO₃ system. *Solid State Ion.* **2004**, *171*, 147–151. [CrossRef]

104. Bocher, L.; Aguirre, M.H.; Logvinovich, D.; Shkabko, A.; Robert, R.; Trottmann, M.; Weidenkaff, A. CaMn₁₋ₓNbₓO₃ (x ≤ 0.08) perovskite-type phases as promising new high-temperature n-type thermoelectric materials. *Inorg. Chem.* **2008**, *47*, 8077–8085. [CrossRef]

105. Zhu, Y.H.; Su, W.B.; Liu, J.; Zhou, Y.C.; Li, J.C.; Zhang, X.H.; Du, Y.L.; Wang, C.L. Effects of Dy and Yb co-doping on thermoelectric properties of CaMnO₃ ceramics. *Ceram. Int.* **2015**, *41*, 1535–1539. [CrossRef]

106. Liu, K.K.; Liu, Z.Y.; Zhang, F.P.; Zhang, J.X.; Yang, X.Y.; Zhang, J.W.; Shi, J.L.; Ren, G.; He, T.W.; Duan, J.J. Improved thermoelectric performance in Pr and Sr Co-doped CaMnO₃ materials. *J. Alloys Compd.* **2019**, *808*, 151476. [CrossRef]

107. Ohtaki, M.; Araki, K.; Yamamoto, K. High thermoelectric performance of dually doped ZnO ceramics. *J. Electron. Mater.* **2009**, *38*, 1234–1238. [CrossRef]

108. Pham, A.T.T.; Luu, T.A.; Pham, N.K.; Thi, H.K.; Nguyen, T.H.; Hoang, D.V.; Lai, H.T.; Tran, V.C.; Park, J.H.; Lee, J.K.; et al. Multi-scale defects in ZnO thermoelectric ceramic materials co-doped with In and Ga. *Ceram. Int.* **2020**, *46*, 10748–10758. [CrossRef]

109. Zhang, D.B.; Zhang, B.P.; Ye, D.S.; Liu, Y.C.; Li, S. Enhanced Al/Ni co-doping and power factor in textured ZnO thermoelectric ceramics prepared by hydrothermal synthesis and spark plasma sintering. *J. Alloys Compd.* **2016**, *656*, 784–792. [CrossRef]

110. Constantinescu, G.; Rasekh, S.; Torres, M.A.; Bosque, P.; Diez, J.C.; Madre, M.A.; Sotelo, A. Effect of Na doping on the Ca₃Co₄O₉ thermoelectric performance. *Ceram. Int.* **2015**, *41*, 10897–10903. [CrossRef]

111. Zhang, L.; Liu, Y.; Tan, T.T.; Liu, Y.; Zheng, J.; Yang, Y.L.; Hou, X.J.; Feng, L.; Suo, G.Q.; Ye, X.H.; et al. Thermoelectric performance enhancement by manipulation of Sr/Ti doping in two sublayers of Ca₃Co₄O₉. *J. Adv. Ceram.* **2020**, *9*, 769–781. [CrossRef]

112. Constantinescu, G.; Rasekh, S.; Torres, M.A.; Madre, M.A.; Sotelo, A.; Diez, J.C. Improvement of thermoelectric properties in Ca₃Co₄O₉ ceramics by Ba doping. *J. Mater. Sci. Mater. Electron.* **2015**, *26*, 3466–3473. [CrossRef]

113. Delorme, F.; Diaz-Chao, P.; Giovannelli, F. Effect of Ca substitution by Fe on the thermoelectric properties of Ca₃Co₄O₉ ceramics. *J. Electroceram.* **2018**, *40*, 107–114. [CrossRef]

114. Demirel, S.; Altin, E.; Oz, E.; Altin, S.; Bayri, A. An enhancement ZT and spin state transition of Ca₃Co₄O₉ with Pb doping. *J. Alloys Compd.* **2015**, *627*, 430–437. [CrossRef]

115. Park, K.; Hakeem, D.A.; Cha, J.S. Synthesis and structural properties of thermoelectric Ca₃₋ₓAgₓCo₄O₉₊δ powders. *Dalton Trans.* **2016**, *45*, 6990–6997. [CrossRef] [PubMed]

116. Constantinescu, G.; Madre, M.A.; Rasekh, S.; Torres, M.A.; Diez, J.C.; Sotelo, A. Effect of Ga addition on Ca-deficient Ca₃Co₄O₉ thermoelectric materials. *Ceram. Int.* **2014**, *40*, 6255–6260. [CrossRef]

117. Saini, S.; Yaddanapudi, H.S.; Tian, K.; Yin, Y.; Magginetti, D.; Tiwari, A. Terbium ion doping in Ca₃Co₄O₉: A step towards high-performance thermoelectric materials. *Sci. Rep.* **2017**, *7*, 44621. [CrossRef]

118. Bhaskar, A.; Huang, Y.C.; Liu, C. Improvement on the low-temperature thermoelectric characteristics of Ca₃₋ₓYbₓCo₄O₉₊δ (0 ≤ x ≤ 0.10). *Ceram. Int.* **2014**, *40*, 5937–5943. [CrossRef]

119. Yang, W.C.; Qian, H.J.; Gan, J.Y.; Wei, W.; Wang, Z.H.; Tang, G.D. Effects of Lu and Ni substitution on thermoelectric properties of $Ca_3Co_4O_{9+\delta}$. *J. Electron. Mater.* **2016**, *45*, 4171–4176. [CrossRef]

120. Wang, Y.; Sui, Y.; Ren, P.; Wang, L.; Wang, X.J.; Su, W.H.; Fan, H.J. Strongly correlated properties and enhanced thermoelectric response in $Ca_3Co_{4-x}M_xO_9$ (M = Fe, Mn, and Cu). *Chem. Mater.* **2009**, *22*, 1155–1163. [CrossRef]

121. Huang, Y.A.; Zhao, B.C.; Lin, S.; Ang, R.; Song, W.H.; Sun, Y.P. Strengthening of thermoelectric performance via Ir doping in layered $Ca_3Co_4O_9$ system. *J. Am. Ceram. Soc.* **2014**, *97*, 798–804. [CrossRef]

122. Ou, Y.; Peng, J.; Li, F.; Yu, Z.X.; Ma, F.Y.; Xie, S.H.; Li, J.F.; Li, J.Y. The effects of dual doping on the thermoelectric properties of $Ca_{3-x}M_xCo_{4-y}Cu_yO_9$ (M = Na, La). *J. Alloys Compd.* **2012**, *526*, 139–144. [CrossRef]

123. Zhang, F.P.; Zhang, X.; Lu, Q.M.; Zhang, J.X.; Liu, Y.Q.; Zhang, G.Z. Preparation and high temperature thermoelectric properties of $Ca_{3-x}Ag_xCo_4O_{9+\delta}$ oxides. *Solid State Ion.* **2011**, *201*, 1–5. [CrossRef]

124. Ito, M.; Nagira, T.; Hara, S. Thermoelectric properties of $Na_xCo_2O_4$ with rare-earth metals doping prepared by polymerized complex method. *J. Alloys Compd.* **2006**, *408*, 1217–1221. [CrossRef]

125. Ito, M.; Furumoto, D. Effects of noble metal addition on microstructure and thermoelectric properties of $Na_xCo_2O_4$. *J. Alloys Compd.* **2008**, *450*, 494–498. [CrossRef]

126. Ito, M.; Furumoto, D. Microstructure and thermoelectric properties of $Na_xCo_2O_4$/Ag composite synthesized by the polymerized complex method. *J. Alloys Compd.* **2008**, *450*, 517–520. [CrossRef]

127. Park, K.; Jang, K.U.; Kwon, H.C.; Kim, J.G.; Cho, W.S. Influence of partial substitution of Cu for Co on the thermoelectric properties of $NaCo_2O_4$. *J. Alloys Compd.* **2006**, *419*, 213–219. [CrossRef]

128. Kurosaki, K.; Muta, H.; Uno, M.; Yamanaka, S. Thermoelectric properties of $NaCo_2O_4$. *J. Alloys Compd.* **2001**, *315*, 234–236. [CrossRef]

129. Akram, R.; Khan, J.; Rafique, S.; Hussain, M.; Maqsood, A.; Naz, A.A. Enhanced thermoelectric properties of single phase Na doped Na_xCoO_2 thermoelectric material. *Mater. Lett.* **2021**, *300*, 130180. [CrossRef]

130. Feng, D.; Zheng, F.S.; Wu, D.; Wu, M.H.; Li, W.; Huang, L.; Zhao, L.D.; He, J.Q. Investigation into the extremely low thermal conductivity in Ba heavily doped BiCuSeO. *Nano Energy* **2016**, *27*, 167–174. [CrossRef]

131. Liu, Y.; Lin, Y.H.; Xu, W.; Cheng, B.; Lan, J.L.; Chen, D.L.; Zhu, H.M.; Nan, C.W. High-temperature transport property of $In_{2-x}Ce_xO_3$ ($0 \leq x \leq 0.10$) fine grained ceramics. *J. Am. Ceram. Soc.* **2012**, *95*, 2568–2572. [CrossRef]

132. Lan, J.L.; Lin, Y.H.; Liu, Y.; Xu, S.L.; Nan, C.W. High thermoelectric performance of nanostructured In_2O_3-based ceramics. *J. Am. Ceram. Soc.* **2012**, *95*, 2465–2469. [CrossRef]

133. Wu, H.J.; Chen, L.L.; Ning, S.T.; Zhao, X.D.; Deng, S.P.; Qi, N.; Ren, F.; Chen, Z.Q.; Tang, J. Extremely low thermal conductivity and enhanced thermoelectric performance of porous Gallium-doped In_2O_3. *ACS Appl. Energy Mater.* **2021**, *4*, 12943–12953. [CrossRef]

134. Zhang, P.; Lou, Z.H.; Gong, L.Y.; Xu, J.; Chen, Q.; Reece, M.J.; Yan, H.X.; Dashevsky, Z.; Gao, F. High-entropy $MTiO_3$ perovskite oxides with glass-like thermal conductivity for thermoelectric applications. *J. Alloys Compd.* **2023**, *937*, 168366. [CrossRef]

135. Zhang, P.; Gong, L.Y.; Lou, Z.H.; Xu, J.; Cao, S.Y.; Zhu, J.T.; Yan, H.X.; Gao, F. Reduced lattice thermal conductivity of perovskite-type high-entropy $(Ca_{0.25}Sr_{0.25}Ba_{0.25}RE_{0.25})TiO_3$ ceramics by phonon engineering for thermoelectric applications. *J. Alloys Compd.* **2022**, *898*, 162858. [CrossRef]

136. Zhang, P.; Lou, Z.H.; Hu, G.X.; Wu, Z.Z.; Xu, J.; Gong, L.Y.; Gao, F. In-situ construction of all-scale hierarchical microstructure and thermoelectric properties of $(Sr_{0.25}Ca_{0.25}Ba_{0.25}La_{0.25})TiO_3$/Pb@Bi composite oxide ceramics. *J. Mater.* 2023; *in press*. [CrossRef]

137. Zhang, R.Z.; Gucci, F.; Zhu, H.Y.; Chen, K.; Reece, M.J. Data-driven design of ecofriendly thermoelectric high-entropy sulfides. *Inorg. Chem.* **2018**, *57*, 13027–13033. [CrossRef]

138. Liu, R.H.; Chen, H.Y.; Zhao, K.P.; Qin, Y.T.; Jiang, B.B.; Zhang, T.S.; Sha, G.; Shi, X.; Uher, C.; Zhang, W.Q.; et al. Entropy as a gene-like performance indicator promoting thermoelectric materials. *Adv. Mater.* **2017**, *29*, 1702712. [CrossRef]

139. Zheng, Y.P.; Zou, M.C.; Zhang, W.Y.; Yi, D.; Lan, J.L.; Nan, C.W.; Lin, Y.H. Electrical and thermal transport behaviours of high-entropy perovskite thermoelectric oxides. *J. Adv. Ceram.* **2021**, *10*, 377–384. [CrossRef]

140. Banerjee, R.; Chatterjee, S.; Ranjan, M.; Bhattacharya, T.; Mukherjee, S.; Jana, S.S.; Dwivedi, A.; Maiti, T. High-entropy perovskites: An emergent class of oxide thermoelectrics with ultralow thermal conductivity. *ACS Sustain. Chem. Eng.* **2020**, *8*, 17022–17032. [CrossRef]

141. Shi, Z.M.; Zhang, J.Z.; Wei, J.; Hou, X.; Cao, S.Y.; Tong, S.J.; Liu, S.Y.; Li, X.T.; Zhang, Y. A-site deficiency improved the thermoelectric performance of high-entropy perovskite manganite-based ceramics. *J. Mater. Chem. C* **2022**, *10*, 15582–15592. [CrossRef]

142. Langenberg, E.; Ferreiro-Vila, E.; Leborán, V.; Fumega, A.O.; Pardo, V.; Rivadulla, F. Analysis of the temperature dependence of the thermal conductivity of insulating single crystal oxides. *APL Mater.* **2016**, *4*, 104815. [CrossRef]

143. Yu, J.C.; Chen, K.; Azough, F.; Alvarez-Ruiz, D.T.; Reece, M.J.; Freer, R. Enhancing the thermoelectric performance of Calcium Cobaltite ceramics by tuning composition and processing. *ACS Appl. Mater. Interfaces* **2020**, *12*, 47634–47646. [CrossRef]

144. Srivastava, D.; Norman, C.; Azough, F.; Schäfer, M.C.; Guilmeau, E.; Kepaptsoglou, D.; Ramasse, Q.M.; Nicotrad, G.; Freer, R. Tuning the thermoelectric properties of A-site deficient $SrTiO_3$ ceramics by vacancies and carrier concentration. *Phys. Chem. Chem. Phys.* **2016**, *18*, 26475–26486. [CrossRef] [PubMed]

145. Lu, Z.L.; Zhang, H.R.; Lei, W.; Sinclair, D.C.; Reaney, I.M. High-figure-of-merit thermoelectric La-doped A-site-deficient $SrTiO_3$ ceramics. *Chem. Mater.* **2016**, *28*, 925–935. [CrossRef]

146. Rahman, J.U.; Nam, W.H.; Van Du, N.; Rahman, G.; Rahman, A.U.; Shin, W.H.; Seo, W.S.; Kim, M.H.; Lee, S. Oxygen vacancy revived phonon-glass electron-crystal in SrTiO₃. *J. Eur. Ceram. Soc.* **2019**, *39*, 358–365. [CrossRef]

147. Bakhshi, H.; Sarraf-Mamoory, R.; Yourdkhani, A.; AbdelNabi, A.A.; Mozharivskyj, Y. Highly dense $Sr_{0.95}Sm_{0.0125}Dy_{0.0125}\square_{0.025}Ti_{0.90}Nb_{0.10}O_{3\pm\delta}/ZrO_2$ composite preparation directly through spark plasma sintering and its thermoelectric properties. *Dalton Trans.* **2020**, *49*, 17–22. [CrossRef]

148. Li, Z.; Xiao, C.; Fan, S.J.; Deng, Y.; Zhang, W.S.; Ye, B.J.; Xie, Y. Dual vacancies: An effective strategy realizing synergistic optimization of thermoelectric property in BiCuSeO. *J. Am. Chem. Soc.* **2015**, *137*, 6587–6593. [CrossRef]

149. Voneshen, D.J.; Refson, K.; Borissenko, E.; Krisch, M.; Bosak, A.; Piovano, A.; Cemal, E.; Enderle, M.; Gutmann, M.J.; Hoesch, M.; et al. Suppression of thermal conductivity by rattling modes in thermoelectric sodium cobaltate. *Nat. Mater.* **2013**, *12*, 1028–1032. [CrossRef]

150. Buscaglia, M.T.; Maglia, F.; Anselmi-Tamburini, U.; Marré, D.; Pallecchi, I.; Ianculescu, A.; Canu, G.; Viviani, M.; Fabrizio, M.; Buscaglia, V. Effect of nanostructure on the thermal conductivity of La-doped SrTiO₃ ceramics. *J. Eur. Ceram. Soc.* **2014**, *34*, 307–316. [CrossRef]

151. Wang, Y.F.; Fujinami, K.; Zhang, R.Z.; Wan, C.L.; Wang, N.; Ba, Y.S.; Koumoto, K. Interfacial thermal resistance and thermal conductivity in nanograined SrTiO₃. *Appl. Phys. Express* **2010**, *3*, 031101. [CrossRef]

152. Ohta, S.; Nomura, T.; Ohta, H.; Koumoto, K. High-temperature carrier transport and thermoelectric properties of heavily La- or Nb-doped SrTiO₃ single crystals. *J. Appl. Phys.* **2005**, *97*, 034106. [CrossRef]

153. Dehkordi, A.M.; Bhattacharya, S.; Darroudi, T.; Graff, J.W.; Schwingenschlogl, U.; Alshareef, H.N.; Tritt, T.M. Large thermoelectric power factor in Pr-Doped $SrTiO_{3-\delta}$ ceramics via grain-boundary-induced mobility enhancement. *Chem. Mater.* **2014**, *26*, 2478–2485. [CrossRef]

154. Dehkordi, A.M.; Bhattacharya, S.; He, J.; Alshareef, H.N.; Tritt, T.M. Significant enhancement in thermoelectric properties of poly-crystalline Pr-doped $SrTiO_{3-\delta}$ ceramics originating from nonuniform distribution of Pr dopants. *Appl. Phys. Lett.* **2014**, *104*, 193902. [CrossRef]

155. Srivastava, D.; Norman, C.; Azough, F.; Schäfer, M.C.; Guilmeau, E.; Freer, R. Improving the thermoelectric properties of SrTiO₃-based ceramics with metallic inclusions. *J. Alloys Compd.* **2018**, *731*, 723–730. [CrossRef]

156. Zhang, P.; Qin, M.J.; Lou, Z.H.; Cao, S.Y.; Gong, L.Y.; Xu, J.; Reece, M.J.; Yan, H.X.; Dashevsky, Z.; Gao, F. Grain orientation evolution and multi-scale interfaces enhanced thermoelectric properties of textured $Sr_{0.9}La_{0.1}TiO_3$ based ceramics. *J. Eur. Ceram. Soc.* **2022**, *42*, 7017–7026. [CrossRef]

157. Jiang, L.; Han, L.H.; Lu, C.H.; Yang, S.Y.; Liu, Y.X.; Jiang, H.Z.; Yan, Y.G.; Tang, X.F.; Yang, D.W. Cu₂Se as textured adjuvant for Pb-doped BiCuSeO materials leading to high thermoelectric performance. *ACS Appl. Mater. Interfaces* **2021**, *13*, 11977–11984. [CrossRef] [PubMed]

158. Chen, Q.; Cao, S.Y.; Song, W.; Xie, Y.; Yan, Z.X.; Xu, J.; Gao, F. Comparing investigation of the anisotropic thermoelectric properties of textured $KSr_2Nb_5O_{15}$ ceramics. *J. Phys. Chem. Solids* **2023**, *175*, 111204. [CrossRef]

159. Shi, Z.M.; Gao, F.; Xu, J.; Zhu, J.H.; Zhang, Y.; Gao, T.; Qin, M.J.; Reece, M.; Yan, H.X. Two–step processing of thermoelectric $(Ca_{0.9}Ag_{0.1})_3Co_4O_9/nano$–sized Ag composites with high ZT. *J. Eur. Ceram. Soc.* **2019**, *39*, 3088–3093. [CrossRef]

160. Zeng, C.C.; Butt, S.; Lin, Y.H.; Li, M.; Nan, C.W. Enhanced thermoelectric performance of $SmBaCuFeO_{5+\delta}/Ag$ composite ceramics. *J. Am. Ceram. Soc.* **2016**, *99*, 1266–1270. [CrossRef]

161. Hinterding, R.; Wolf, M.; Jakob, M.; Oeckler, O.; Feldhoff, A. Improved thermoelectric properties in ceramic composites based on $Ca_3Co_4O_9$ and $Na_2Ca_2Nb_4O_{13}$. *Open Ceram.* **2021**, *8*, 100198. [CrossRef]

162. Jana, S.S.; Maiti, T. Enhanced thermoelectric performance in oxide composites of La and Nb codoped SrTiO₃ by using graphite as the electron mobility booster. *ACS Appl. Mater. Interfaces* **2022**, *14*, 14174–14181. [CrossRef] [PubMed]

163. Bolotin, K.I.; Sikes, K.J.; Jiang, Z.; Klima, M.; Fudenberg, G.; Hone, J.; Kim, P.; Stormer, H.L. Ultrahigh electron mobility in suspended graphene. *Solid State Commun.* **2008**, *146*, 351–355. [CrossRef]

164. Ekren, D.; Cao, J.Y.; Azough, F.; Kepaptsoglou, D.; Ramasse, Q.; Kinloch, I.A.; Freer, R. Controlling the thermoelectric behavior of La-doped SrTiO₃ through processing and addition of graphene oxide. *ACS Appl. Mater. Interfaces* **2022**, *14*, 53711–53723. [CrossRef]

165. Dey, P.; Jana, S.S.; Anjum, F.; Bhattacharya, T.; Maiti, T. Effect of semiconductor to metal transition on thermoelectric performance in oxide nanocomposites of $SrTi_{0.85}Nb_{0.15}O_3$ with graphene oxide. *Appl. Mater. Today* **2020**, *21*, 100869. [CrossRef]

166. Zavjalov, A.; Tikhonov, S.; Kosyanov, D. TiO₂-SrTiO₃ biphase nanoceramics as advanced thermoelectric materials. *Materials* **2019**, *12*, 2895. [CrossRef]

167. Skomedal, G.; Vehus, T.; Kanas, N.; Singh, S.P.; Einarsrud, M.A.; Wiik, K.; Middleton, P.H. Long term stability testing of oxide unicouple thermoelectric modules. *Mater. Today* **2019**, *8*, 696–705. [CrossRef]

168. Shi, X.L.; Zou, J.; Chen, Z.G. Advanced thermoelectric design: From materials and structures to devices. *Chem. Rev.* **2020**, *120*, 7399–7515. [CrossRef]

169. Shin, H.S.; Lee, J.S.; Jeon, S.G.; Yu, J.; Song, J.Y. Thermopower detection of single nanowire using a MEMS device. *Measurement* **2014**, *51*, 470–475. [CrossRef]

170. Lim, C.H.; Choi, S.M.; Seo, W.S.; Lee, M.H.; Lee, K.H.; Park, H.H. A study of electrodes for thermoelectric oxides. *Electron. Mater. Lett.* **2013**, *9*, 445–449. [CrossRef]

171. Choi, S.M.; Lee, K.H.; Lim, C.H.; Seo, W.S. Oxide-based thermoelectric power generation module using p-type $Ca_3Co_4O_9$ and n-type $(ZnO)_7In_2O_3$ legs. *Energ. Convers. Manag.* **2011**, *52*, 335–339. [CrossRef]

172. Funahashi, R.; Matsumura, Y.; Urata, T.; Hiroyo, M.; Hitomi, I.; Shinya, S.; Shigeaki, S. Relationship between tensile strength and durability of oxide thermoelectric modules. *J. Electron. Mater.* **2021**, *50*, 3996–4005. [CrossRef]
173. Tougas, I.M.; Amani, M.; Gregory, O.J. Metallic and ceramic thin film thermocouples for gas turbine engines. *Sensors* **2013**, *13*, 15324–15347. [CrossRef] [PubMed]
174. Yakaboylu, G.A.; Pillai, R.C.; Sabolsky, K.; Sabolsky, E.M. Fabrication and thermoelectric characterization of transition metal silicide-based composite thermocouples. *Sensors* **2018**, *18*, 3759. [CrossRef] [PubMed]
175. Saini, S.; Mele, P.; Miyazaki, K.; Tiwari, A. On-chip thermoelectric module comprised of oxide thin film legs. *Energy Convers.* **2016**, *114*, 251–257. [CrossRef]
176. Tian, Z.; Wang, J.; Yaer, X.; Kang, H.J.; Wang, X.H.; Liu, H.M.; Yang, D.Z.; Wang, T.M. Pencil painting like preparation for flexible thermoelectric material of high-performance p-type $Na_{1.4}Co_2O_4$ and novel n-type $Na_xCo_2O_4$. *J. Mater.* **2021**, *7*, 1153–1160. [CrossRef]
177. Repaka, D.V.M.; Suwardi, A.; Kumar, P. New paradigm for efficient thermoelectrics. In *Energy Saving Coating Materials*; Elsevier: Amsterdam, The Netherlands, 2020; pp. 183–196.
178. Kraemer, D.; Poudel, B.; Feng, H.P.; Caylor, J.C.; Yu, B.; Yan, X.; Ma, Y.; Wang, X.W.; Wang, D.Z.; Muto, A.; et al. High-performance flat-panel solar thermoelectric generators with high thermal concentration. *Nat. Mater.* **2011**, *10*, 532–538. [CrossRef]
179. Ohta, H.; Kim, S.W.; Mune, Y.; Mizoguchi, T.; Nomura, K.; Ohta, S.; Nomura, T.; Nakanishi, Y.; Ikuhara, Y.; Hirano, M.; et al. Giant thermoelectric Seebeck coefficient of a two-dimensional electron gas in $SrTiO_3$. *Nat. Mater.* **2007**, *6*, 129–134. [CrossRef]
180. Trocha, P.; Siuda, E. Spin-thermoelectric effects in a quantum dot hybrid system with magnetic insulator. *Sci. Rep.* **2022**, *12*, 5348. [CrossRef]